Check for updates

Surface functionalization of MXenes

Mohammad Mozafari [ID] and Masoud Soroush [ID]*

MXenes, a new family of two-dimensional (2D) transition metal carbides and nitrides, have received great research attention in diverse applications, including biomedicine, sensing, catalysis, energy storage and conversion, adsorption, and membrane-based separation, owing to their extraordinary physicochemical properties and various chemical compositions. In recent years, many surface functionalization strategies, such as surface-initiated polymerization and single heteroatom doping, have been cleverly developed to expand the potential of MXenes in different fields. This article reviews and puts into perspective the recent advances in MXene surface functionalization and various applications of the modified MXenes. The effect of surface functionalization on MXene properties (such as electronic, magnetic, mechanical, optical, and hydrophilicity/hydrophobicity) is discussed. Potential applications of pristine and functionalized MXenes in different fields are discussed. Finally, challenges and future directions in MXene surface modification are examined.

1. Introduction

In recent years, two-dimensional (2D) nanomaterials, such as MXenes, black phosphorus nanosheets, molybdenum disulfide, and graphene, have received considerable attention[1–4] due to their unique structures and attractive chemical and physical properties. As such, they have shown potential for various applications in the fields of biomedicine, sensing, environment, and energy.[5–8] In particular, MXenes have received considerable attention around the world.[9,10] The first discovered MXene (Ti_3C_2) was synthesized by selective etching of Al elements using hydrofluoric acid (HF).[11] The general chemical formula of MXenes is $M_{n+1}X_nT_x$ (n = 1–4), where M, X, and T represent an early transition metal (including Mo, Nb, Cr, V, Ti, and Hf), carbon or nitrogen, and surface functional groups, respectively.[10,12,13] The integer x is the number of functional groups.[11] While many MXenes with various compositions have been proposed, only a limited number of them have been synthesized. The diversity of MXene compositions implies that a variety of MXenes with desired properties can be synthesized.[14,15] The chemical formula of the reactant, the MAX phase (as a kind of ternary ceramic material), from which a MXene is synthesized, is $M_{n+1}AX_n$, which has a layered hexagonal structure.[16] The MAX phase is formed by covalent bonds between the M and X atoms, and the M–X layer is alternately ordered with an A atomic layer *via* a metallic bond between A and M, although M–A bonds are weaker compared to M–X bonds.[17]

Owing to their promising mechanical, chemical, and physical properties, and large surface area,[18] MXenes are being applied in various applications such as adsorption,[19–21] membrane separation,[22–25] catalysis,[26,27] energy storage,[28–30] sensing,[26,31–33] and biomedicine.[34–36] Furthermore, the existence of many functional groups such as oxygen (–O), fluorine (–F), hydroxyl (–OH), and chloride (–Cl) on their surface allows for their surface functionalization, which increases their versatility further.[37–40] For example, adsorption of metal ions was investigated using –O-containing composites of Ti_3C_2, which were produced by the conversion of –OH groups on their surface.[41] Besides, because of their extraordinary biocompatibility,[42] MXenes have shown great potential for biomedical applications.

Different methods of synthesizing MXenes have been introduced.[43] They include (i) top-down methods (selective etching of MAX and non-MAX phases),[44,45] (ii) bottom-up methods (chemical vapor deposition (CVD) and salt-templated growth), and (iii) chemical transformations. The single-layer and multi-layer nanostructure of MXenes can be manufactured using these methods. On the other hand, poor stability in the presence of molecular oxygen, easy restacking, and low mechanical flexibility are the disadvantages of MXenes that have limited the applications of pristine MXenes.[46–49] Despite the numerous merits of MXenes, they still lack properties needed in several fields.[50] Additionally, pristine MXenes tend to precipitate and accumulate in water due to their poor water dispersibility.[51] Hence, the surface functionalization and modification can substantially enhance their performance and stability.[52]

Generally, the surface properties of MXenes can be modified and improved by the type and fraction of the T group during the production process.[53] Recently, functionalized MXenes have

Department of Chemical and Biological Engineering, Drexel University, Philadelphia, PA 19104, USA. E-mail: soroushm@drexel.edu

been synthesized by surface modification of pristine MXenes with covalent and non-covalent modifications. The non-covalent surface modification is obtained by a combination of van der Waals forces, hydrogen bonding, and electrostatic attraction.[35,54–57] Covalent surface functionalization methods are classified into three groups:[58–60] (i) those that involve small molecules such as alkali metal hydroxides, acid halide or acid anhydride, epoxy compounds, and organic amines,[61–64] (ii) those that involve surface-initiated polymerization by macromolecules,[65,66] and (iii) those that involve single heteroatoms.[16]

In this article, recent developments in the functionalization of MXenes are reviewed. First, strategies for MXene surface functionalization are reviewed and discussed. The properties of the surface modified MXenes and their potential applications in separation, biomedical, sensing, energy storage and conversion, and catalysis are discussed. Finally, the future perspective of functionalized MXenes, and challenges and opportunities in this field are highlighted.

2. Methods of surface functionalization

Plentiful –OH and –O containing groups on the surface of MXenes can be utilized as active sites for covalent binding by means of controlling the surface terminations, surface-active initiators, small molecules, and polymers.[67–71] The performance of MXenes can be enhanced easily by suitable functional groups because of the hydrophilic nature of MXenes.[16] Many have studied the chemical surface functionalization of MXenes. Table 1 lists the various modified MXenes and the surface-functionalization methods used to prepare them.

2.1. Controlling surface terminations

The surface modification of MXenes through controlling the T groups allows for adjusting the physical properties of MXenes, including the concentrations and types of electrochemical active sites and electronic structures.[83] –O and –F surface terminations can be easily achieved by conventional etching techniques such as fluoride-containing salts or HF. More importantly, the concentrations and types of surface terminations can be tuned by adjusting the etching time and the concentration of etchants, and using various post-treatments such as hydrazine and annealing in diverse atmospheres.[84,85] For instance, Schultz et al. studied the effect of various surface terminations on the physical properties.[86] Their measurement of the electronic structure indicated that Ti_3C_2 has a high (above 1 eV) dispersion due to its Ti–O bonds. Annealing at 380 °C in vacuum increases the work function from 3.9 to 4.8 eV, because of the desorption of –OH species, contaminants, and water. The work function decreased to 4.1 eV with fluorine desorption at higher temperatures from 500 to 750 °C. Moreover, density functional theory (DFT) has been used to evaluate the effect of surface terminations on the electronic conductivity.[87] It was found that the Fermi level density of states (DOS) of an MXene is affected by surface terminations. The concentration of –F terminations decreased by annealing Ti_3C_2 from 300 to 775 °C, which was supported by measurements from in situ electron energy loss spectroscopy (Fig. 1a). The significant enhancement of electronic conductivity was ascribed to the decrease of –F terminations during annealing at 700–775 °C (Fig. 1b). Furthermore, Tang et al. investigated the saturation magnetization of Ti_3C_2 through Ti–C vacancy production under H_2 annealing.[88] They showed a similar level of –O concentration after annealing in H_2 from 100 to 500 °C, while the C–Ti–OH functional groups transformed to O–Ti–O and C–Ti–O. The Ti–C vacancy with C and Ti vacancies formed in the annealing process (Fig. 1c). The fully terminated Ti_3C_2 MXenes were theoretically nonmagnetic, while the pristine Ti_3C_2 was ferromagnetic. The influence of Ti–C vacancy on the improvement of saturation magnetization was clearly confirmed from DFT calculations and magnetization enhancement (Fig. 1d).

2.2. Small molecules

Performance characteristics of MXenes such as mechanical stability, electrical properties, and solution stability can be

Table 1 Surface-modified MXenes and their methods of preparation

Surface functionalized 2D MXenes	Sample	Synthesis method	Solvent or atmosphere reaction	Temperature (°C)	Ref.
Functionalized MXenes by small molecules	$NaAlH_4$-modified Ti_3C_2	Ball milling	Ar	—	72
	FePc-modified Ti_3C_2	Self-assembly	Dimethylformamide (DMF)	—	54
	$C_{12}E_6$-modified Ti_3C_2	Sonication	Water	40	55
	Et-modified Nb_2C	Hydrothermal approach	Ethanol	100	73
Functionalized MXenes by macromolecules	Sodium alginate modified Ti_3C_2	Vacuum-assisted filtration	Deionized water	Room temperature	74
	PPy modified Ti_3C_2	In situ polymerization	Deionized water	Room temperature	65
	PS modified Ti_3C_2	Electrostatic assembly	Deionized water	50	75
	PVA modified Ti_3C_2	Vacuum-assisted filtration	Deionized water	Room temperature	76
	PDDA modified Ti_3C_2	Vacuum-assisted filtration	Deionized water	Room temperature	76
Functionalized MXenes by single heteroatoms	V-Doped Ti_3C_2	Hydrothermal approach	Water	120	77
	S-Doped Ti_3C_2	Solution blending	Deionized water	155	78
	S-Doped Ti_3C_2	Heat and milling treatment	Ar	1650	79
	N-Doped V_4C_3	Heat treatment	Ammonia	350–550	80
	N-Doped Nb_2C	Hydrothermal approach	Deionized water	150	81
	P-Doped V_2C	Heat treatment	Ar	300–500	82
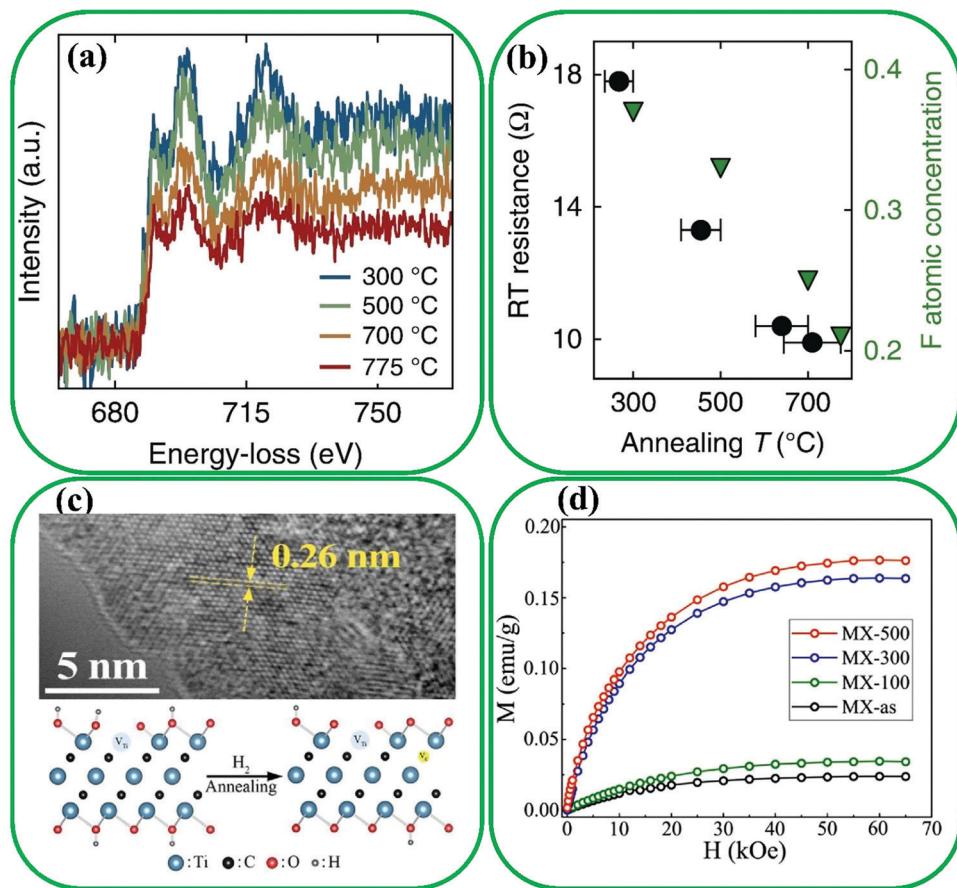
**Fig. 1** Effect of surface terminations on the conductivity of MXenes; (a) loss of −F terminations under annealing by *in situ* electron energy loss spectroscopy of Ti_3C_2, and (b) comparison of −F concentration (green triangles) and the post-anneal room temperature resistance of Ti_3C_2 (black circles). Reproduced with permission.[87] Copyright 2019, Nature. (c) Representation scheme and high-resolution transmission electron microscopy of structural evolution after annealing in H_2, and (d) indicating the comparison of magnetic properties as a function of the applied field H measured at 2 K. Reproduced with permission.[88] Copyright 2020, Elsevier.

further enhanced by surface modification of MXenes with a variety of small molecules, which are easy to process and are inexpensive.[61,63] To illustrate, Xia *et al.* introduced a non-ionic surfactant, hexaethylene glycol monododecyl ether ($C_{12}E_6$), on the surface of Ti_3C_2 MXenes ($C_{12}E_6@Ti_3C_2$) to improve molecular interactions, resulting in enhanced packing symmetry (Fig. 2a).[55] In the $C_{12}E_6@Ti_3C_2$ composite, strong hydrogen bonds are formed between the −O or −F groups on the MXene's surface and the −OH groups of $C_{12}E_6$. A novel fan-like texture under an optical microscope was used to confirm the introduction of $C_{12}E_6$ between MXene nanosheets (Fig. 2b). In addition, a one-step direct reaction of Ti_3C_2 sheets with diazonium salt was reported by Lei *et al.* who prepared a sulfonic functionalized MXene, denoted as Ti_3C_2–SO_3H.[89] The results of SEM characterization demonstrated that the pristine Ti_3C_2 MXenes have packed stacked lamellar layered structures. By contrast, granular structures can be seen on the surface of Ti_3C_2–SO_3H (Fig. 2c and d). Jin *et al.* used a simple solvothermal/hydrothermal method to modify the surface of Nb_2C MXenes for developing the electromagnetic wave (EMW) absorbing performance.[73] Deionized (DI) water or ethanol (Et) was used in the

solvothermal treatment process instead of DMF. The results presented superior EMW performance for Et-treated Nb_2C MXenes because of increased surface functional groups, enlarged interlayer spacing, and improved dielectric loss. Larger interlayer spacing can lead to multiple reflections between Nb_2C sheets, resulting in enhanced EMW absorption. In addition, the functional groups on the edge and surface of Nb_2C can act as polarization sites to attenuate the energy of EMW.

In addition, Yang *et al.* were able to increase the molecular interactions of MXene nanosheets using hexaethylene glycol monododecyl ether ($C_{12}E_6$) as a non-ionic surfactant.[55] MXenes have also been functionalized using other small molecules such as bismuth ferrite ($BiFeO_3$)[92,93] and sodium aluminum hydride ($NaAlH_4$).[94] A chemical coupling method was applied to produce amino groups on the MXene's surface (Fig. 2e), and the resultant functionalized MXene nanosheets can be used as a platform to immobilize different biomolecules.[90] To conduct large-scale delamination of MXenes, Wang *et al.* developed a method of diazonium surface chemistry,[61] which weakens the M–X bonds and expands the interlayer spacing by the formation of aryl-surface linkage using diazonium and sulfanilic
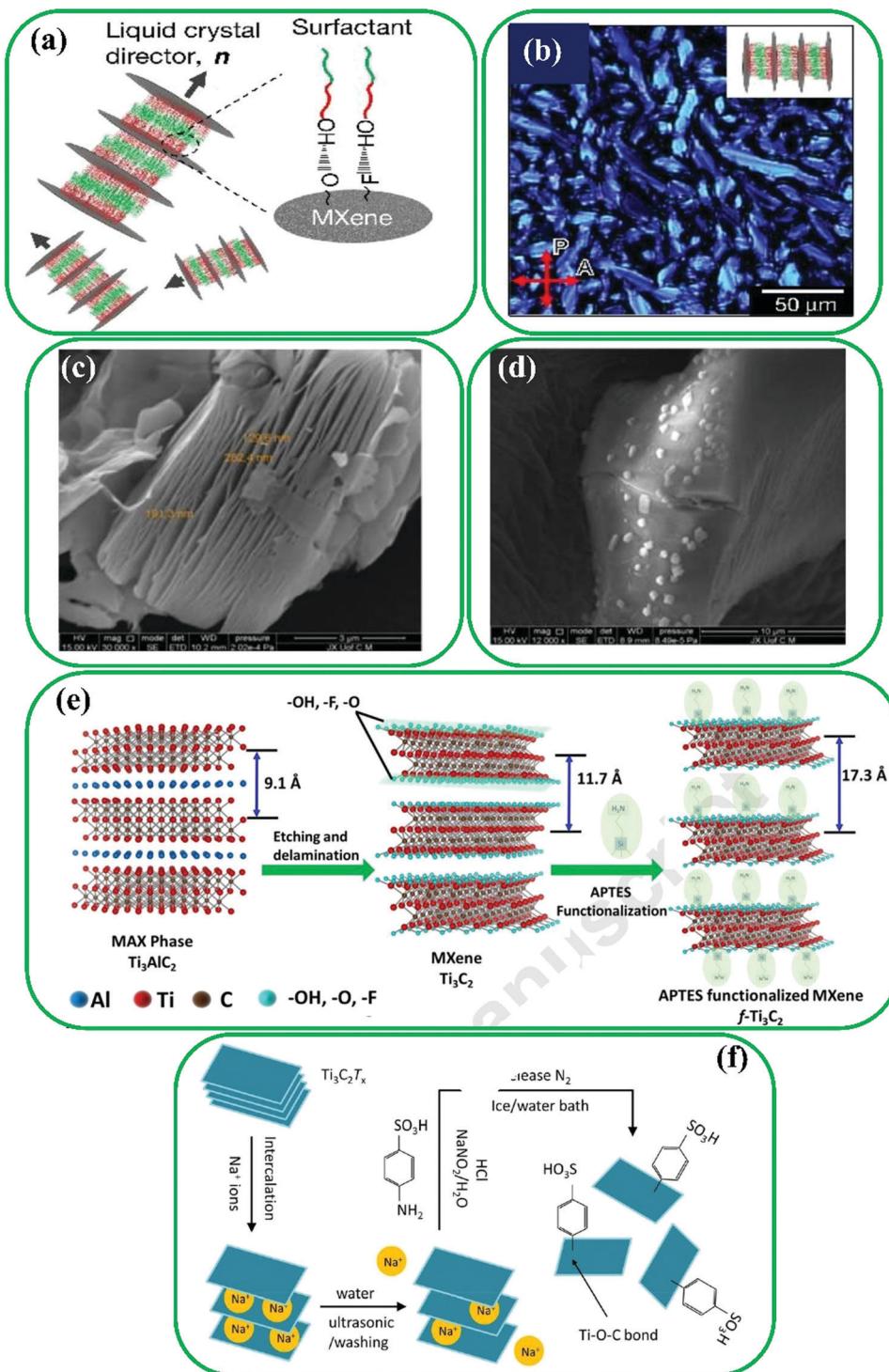
Fig. 2 (a) Schematic illustration of the $C_{12}E_6$-improved lamellar structure of Ti_3C_2 MXenes. (b) The fan-like texture of the lamellar phase of Ti_3C_2 MXenes. Reproduced with permission.[55] Copyright 2018, Nature. SEM images of (c) pristine Ti_3C_2 sheets and (d) Ti_3C_2–SO_3H. Reproduced with permission.[89] Copyright 2019, Elsevier. (e) Preparation of Ti_3C_2 MXenes by Al etching and surface modification of Ti_3C_2 MXenes. Reproduced with permission.[90] Copyright 2018, Elsevier. (f) Surface modification of Ti_3C_2 MXene with diazonium ion. Reproduced with permission.[91] Copyright 2018, Elsevier.

salts. In another study, diazonium ions were used for the *in situ* modification of the MXene's surface,[91] as shown in Fig. 2f, where it is proven that the covalent grafting of $C_6H_4SO_3H$ groups on the surface of Ti_3C_2 improves the electrical properties.

It should be noted that the –OH groups on the MXene's surface can react with trimesoyl chloride, epichlorohydrin, and silane agents to conduct etherification and esterification.[95,96] During the production of MXene/cellulose hydrogels, epichlorohydrin served

as a cross-linker between MXenes and cellulose *via* the formation of covalent bonds with the existing –OH groups on the surface of MXenes.

2.3. Surface-initiated polymerization

The numerous active functional groups on the surface of MXenes allow polymers to be *ex situ* blended or *in situ* polymerized.[65,74,83,97–101] MXene/polymer composites are usually produced using an *ex situ* blending approach, which provides some merits such as well-defined polymer structures and tunable compositions. Hence, the interaction between polymers and MXenes can be efficiently improved by hydrogen bonding[102] and electrostatic interactions.[75,76] For instance, Sun *et al.* produced highly conductive MXene@polystyrene (PS) nanocomposites (MXene@PS) using the electrostatic assembling of positive PS and negative MXene nanosheets, followed by compression molding (Fig. 3a).[75] Fig. 3b shows the perfect and clean microstructure core–shell MXene@PS hybrid. The abundant functional groups (–F, –O, and –OH) on the surface of MXenes allow them to assemble on the PS by van der Waals forces, hydrogen bonding, and electrostatic interactions. At lower contents of Ti_3C_2 MXenes, assembling occurred through electrostatic interactions, whereas at higher contents, the van der Waals forces and hydrogen bonds

are the main driving forces for the assembling of Ti_3C_2 MXenes on the surface of the PS. In addition, Ling *et al.* reported the fabrication of two Ti_3C_2/polymer composites: Ti_3C_2/polyvinyl alcohol (PVA) and Ti_3C_2/polydiallyldimethylammonium (PDDA) (Fig. 3c).[76] A PVA/Ti_3C_2 composite can be easily obtained by hydrogen bonding owing to the abundant hydrogel groups on the structure of PVA. As Ti_3C_2 MXenes are negatively charged flakes and PDDA is a cationic polymer, the PDDA/Ti_3C_2 composite can be easily formed by electrostatic interactions. The TEM image of the PVA/Ti_3C_2 composite (Fig. 3e) clearly shows the intercalation of PVA layers, and Fig. 3d shows the orderly stacked layers of the PDDA/Ti_3C_2 composite formed by vacuum-assisted filtration.

Strong covalent bonds between MXenes and polymers can be formed *via in situ* polymerization with monomers such as ε-caprolaction[103] and pyrrole.[65,104] For example, Boota *et al.* developed a method for *in situ* polymerization of pyrrole between Ti_3C_2 layers[65] (Fig. 4a). As shown in Fig. 4b, a periodic pattern was produced, which can be ascribed to the well-aligned polypyrrole (PPy) between Ti_3C_2 layers along with appropriate intercalation of PPy chains. In the case of PPy/Ti_3C_2 composites, the interaction between Ti_3C_2 and polymer chains is formed by hydrogen bonds between the –O groups on
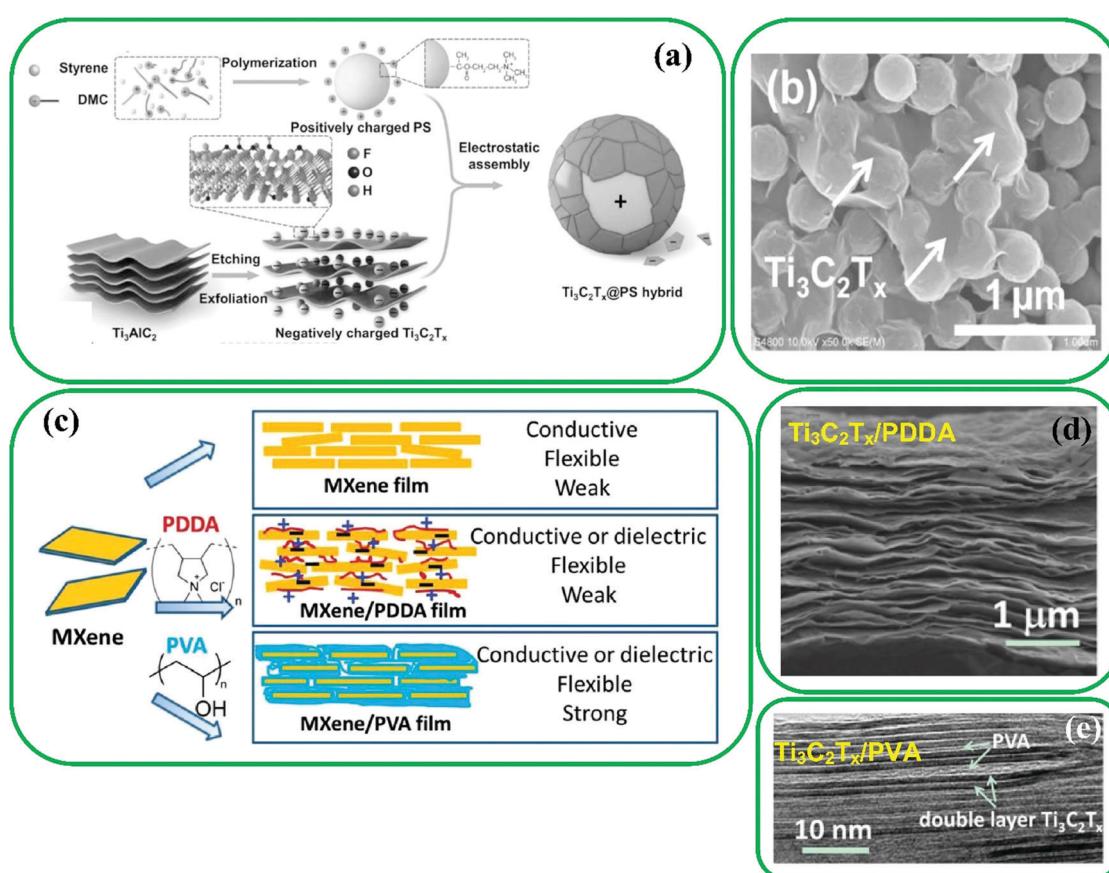

Fig. 3 (a) Schematic representation of the synthesis of MXene@PS hybrid. (b) SEM image of MXene@PS hybrid. Reproduced with permission.[75] Copyright 2017, Wiley. (c) MXene modification with charged PDDA and electrically neutral PVA, (d) cross-sectional image of PDDA/Ti_3C_2, and (e) high-resolution TEM image of PVA/Ti_3C_2 composite. Reproduced with permission.[76] Copyright 2014, National Acad. Sciences.

the surface of Ti_3C_2 and the H and N of PPy. Moreover, soybean phospholipid (SP) consists of biomacromolecules that are extensively used for surface functionalization due to their biocompatible characteristics.[16] Lin *et al.* reported that surface functionalization of Ti_3C_2 with SP (Fig. 4c)[35] improves blood circulation and biodistribution in tumors in physiological environments. Furthermore, enhanced stability of MXenes in physiological solutions was observed using poly(ethylene glycol) (PEG).[105]

Polydopamine (PDA) is another suitable agent for MXene surface modification, because there are abundant amino and catechol groups in its backbone, which can form non-covalent and covalent interactions with organic and inorganic surfaces.[60,107] To produce a Ti_3C_2@carbon nanotube (CNT) composite, cobalt was adsorbed on the surface of Ti_3C_2, and CNTs were then formed after the formation of PDA layers on the surface of Ti_3C_2.[16] The capacitive performance of Ti_3C_2 improved with PDA modification.[108]

Surface-initiated polymerization is another method for surface functionalization of MXenes. For instance, Fig. 4d illustrates the surface-initiated polymerization of V_2C with poly(2-(dimethylamino)ethyl methacrylate) (PDMAEMA) using –OH groups as a photoactive site.[98] Additionally, a peroxide decoration method was reported by Tao *et al.*, where the –OH acts as an initiator for surface polymerization of monomers.[106] Polymerization occurs by adding nitrogen to a mixture of an MXene and an acrylic monomer (Fig. 4e). The surface functionalization with macromolecules is a promising strategy to improve MXenes' pristine properties tailored for various applications.

Furthermore, strong bonds between inorganic and organic groups can be made by silane reagents with different functional groups such as phenyl, chloro, vinyl, epoxy, methacrylate, amine, and diamine.[13] Silanol groups can be obtained by the hydrolysis of alkoxy groups and the presence of water and moisture on the surface of nanomaterials, which can cause the formation of covalent bonds between the silanol groups and available –OH groups on the surface of nanomaterials by a dehydration reaction. Amino-silane functionalization of TiO_2 was reported by Shamsabadi *et al.*,[109] which inspired the amino-silane modification of Ti_3C_2 by the same group[13] because of the similarity of –OH groups in TiO_2 nanoparticles and Ti_3C_2. [3-(2-Aminoethylamino)propyl]trimethoxysilane (AEAPTMS) was grafted on the surface of Ti_3C_2 *via* chemical reactions between the –OH groups of Ti_3C_2 and AEAPTMS: the amine group ends leading to electrostatic interactions, and the silanol group ends leading to covalent bonding (Fig. 4f). By amino functionalization of MXene materials, numerous opportunities of subsequent reactions are created. These include reactions with curing agents for epoxy resins and surface-initiated atom transfer radical polymerization due to the existence of free amine groups. These reactions make MXene materials suitable for use in energy-storage devices, electrochemical biosensors, fuel cells, catalysis, metal-ion batteries, antibacterial coating, drug delivery, and dye adsorbents.[110–114]

2.4. Single heteroatom method

The use of MXenes in Na-ion batteries (NIBs) and Li-ion batteries (LIBs) is still challenging[115] because of their unfavorable electrochemical properties, which can be addressed by increasing the interlayer spacing of MXenes *via* single heteroatoms.[116] Significant improvement in the electrochemical performance of MXenes has been obtained using P, S, and N doping approaches.[81,82,117,118] For instance, N-doped Nb_2C MXene was produced by Liu *et al.* by means of a hydrothermal method.[81] The layered structure of N-doped Nb_2C can be seen in Fig. 5a, where it can be concluded that the morphology of Nb_2C does not change with N-doping, as confirmed by the uniform distribution of C, O, and Nb elements (Fig. 5b). Furthermore, p-doped V_2C was synthesized by Yoon *et al.* using heat treatment *via* triphenylphosphine (TPP). p-Doped V_2C with a large interlayer spacing (1.03 nm) was obtained, while pristine V_2C had an interlayer spacing of 0.97 nm (Fig. 5c). Besides, N-doped V_2C with different N contents was produced, as the heat treatment temperature was varied from 350 to 550 °C. The N-doped V_2C was produced by annealing in an ammonia atmosphere, resulting in the uniform distribution of elements (such as N, C, and V). Other recent efforts to enhance the performance of MXenes include the syntheses of cation (NH^{4+}, Al^{3+}, Mg^{2+}, Ca^{2+}, and K^+)-doped Ti_3C_2, germanium- and silicon-doped $Sc_2C(OH)_2$,[119] boron-doped W_2CO_2 and Mo_2CO_2,[120] and palladium/platinum-doped Nb_2C.[121]

3. Effects of surface functionalization on MXene properties

3.1. Electronic properties

MXenes have shown diverse electronic properties such as semiconductivity, metallicity, and topological insulativity, owing to their flexible thickness tunability, different surface functionalization possibilities, and various compositions.[122,123] It should be noted that the electronic characteristics of MXenes can be improved by surface modification.[124–126] However, as most MXenes are metallic,[127] their electronic properties are mainly determined by the M atoms. As has been predicted, the Mo- and W-based MXenes are insulators.[128,129] Some metallic MXenes may become semiconductors after surface modification.[130] For instance, F- and I-terminated Ti_3C_2 have shown semiconductivity, while pristine Ti_3C_2[131] has metallic properties.

Dong *et al.* reported Hf_2VC_2, Hf_2MnC_2, and Ti_2MnC_2 MXenes (Fig. 6a and b).[132] Ti_2MnC_2 is metallic or a semiconductor based on the type of the functional groups. For example, it is a semiconductor with –O terminations. Moreover, Du *et al.* reported that some metallic MXenes with –OH and –O terminations (such as Nb_4C_3, Ti_3C_2, Nb_2C, V_2C, and Ti_2C) have shown significant charge transfer,[133] while Ti_3CO_2 exhibited semiconductor properties due to the generation of a large gap induced by the downshifting of the Fermi level (Fig. 6c). In $TiCO_2$, by increasing the donation of electrons between carbon, oxygen, and titanium atoms, the Fermi level decreases. This phenomenon was confirmed by another study by Pandey *et al.* which evaluated the electronic properties of $M_nC_{n-1}O_2$ MXenes ($n = 2$, 3, 4, and M = W, Ta, Hf, Mo, Nb, Zr, Y, Mn, Cr, V, Ti, Sc).[134] Apart from several O-terminated MXenes, including $Hf_3C_2O_2$, Hf_2CO_2, $Zr_3C_3O_2$, $ZrCO_2$, and $TiCO_2$, other F- or OH-terminated
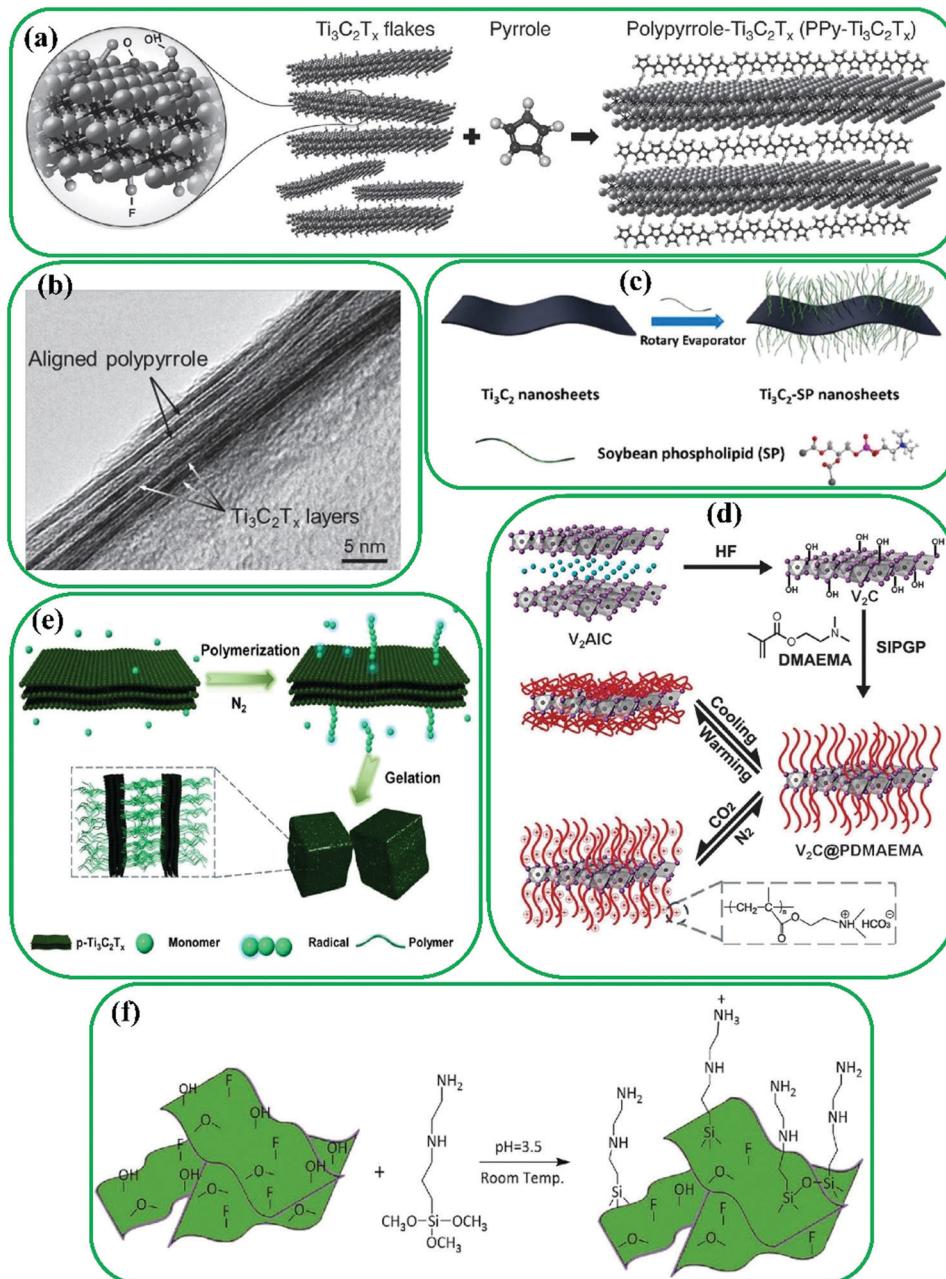
Fig. 4 (a) *In situ* surface polymerization of Ti_3C_2 with pyrrole, and (b) cross-sectional image of PPy/Ti_3C_2 composites indicating well aligned PPy chains between Ti_3C_2 layers. Reproduced with permission.[65] Copyright 2016, Wiley. (c) Illustration of surface functionalization of Ti_3C_2 with SP. Reproduced with permission.[35] Copyright 2017, American Chemical Society. (d) Synthesis of $V_2C@PDMAEMA$. Reproduced with permission.[98] Copyright 2015, The Royal Society of Chemistry. (e) p-Ti_3C_2-initiated polymerization and alternative gelation. Reproduced with permission.[106] Copyright 2019, The Royal Society of Chemistry. (f) Schematic illustration of Ti_3C_2 flake functionalization process with AEAPTMS (coupling agent). Reproduced with permission.[13] Copyright 2020, Wiley.

MXenes were metallic. Furthermore, the electronic properties of i-MAX phases, such as $(V_{2/3}Zr_{1/3})_2AlC$, $(W_{2/3}Y_{1/3})_2AlC$, $(W_{2/3}Sc_{1/3})_2AlC$, $(Mo_{2/3}Y_{1/3})_2AlC$, and $(Mo_{2/3}Y_{1/3})_2AlC$, have been studied.[135] The pristine MXenes synthesized from $(Mo_{2/3}Y_{1/3})_2AlC$ and OH- and F-terminated of $(Mo_{2/3}Y_{1/3})_2C$ are metallic, while the O-terminated sample becomes a semi-conductor (Fig. 6d). Chen *et al.* investigated the conductivity properties of pristine Ti_3C_2 and Ti_3C_2/glycine hybrid.[54] Their results (Fig. 6e) indicated that the conductivity of the

hybrid diminished by increasing the amount of poor conductive glycine in the hybrid.

In addition to experimental studies, theoretical studies have also been performed recently to assess the DOS, band structure, and electronic properties of pristine and functionalized MXenes.[136] As examples, several MXenes such as Hf_2CO_2, Zr_2CO_2, Ti_2CO_2, and Sc_2CT_x (T = O, F, OH) were reported with a band gap ranging from 0.24 to 1.8 eV,[130] which shows the remarkable effect of the surface groups of MXenes (Fig. 7a).
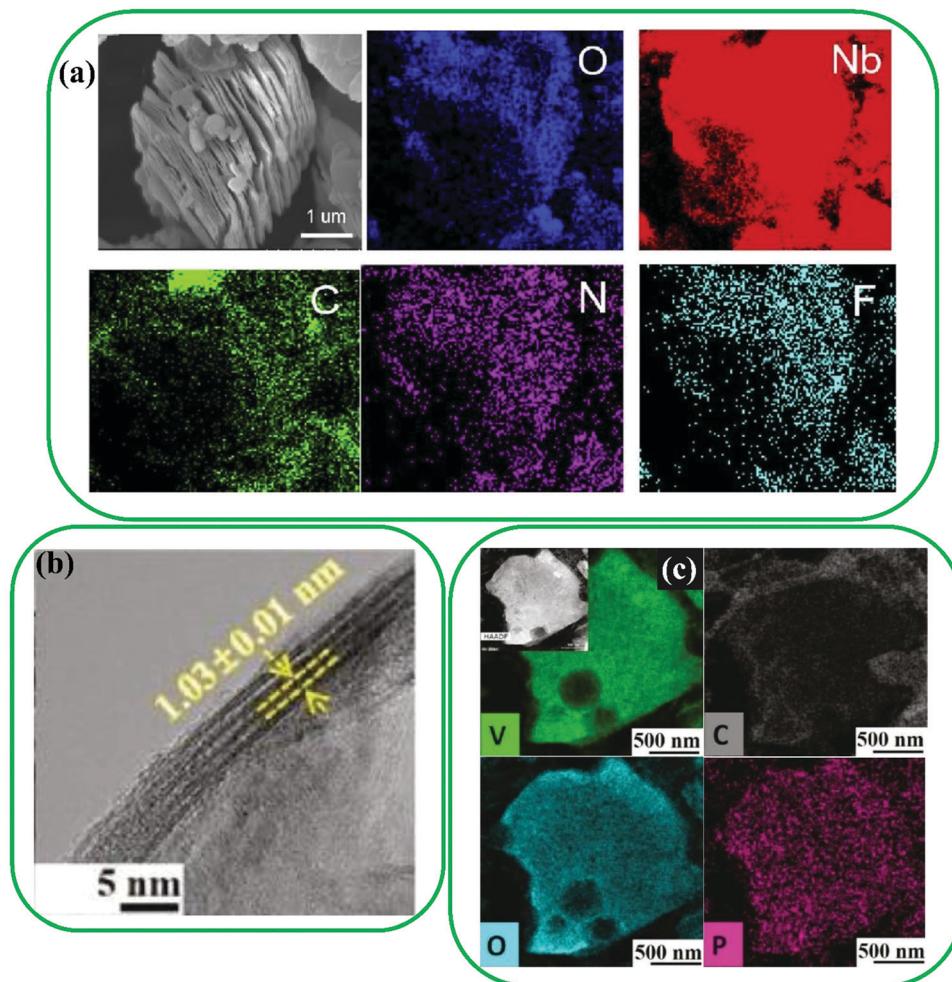
Fig. 5 (a) A SEM image and corresponding EDS mapping images of N-doped Nb₂C MXene. Reproduced with permission.[81] Copyright 2019, Elsevier. (b) A TEM image and (c) EDS mapping images of P-doped V₂C MXene. Reproduced with permission.[82] Copyright 2019, Wiley.

The band structure of Sc_2CO_2 is different from those of Sc_2CF_2 and $Sc_2C(OH)_2$, and this remarkable effect can be ascribed to the fact that an –OH or –F group is stabilized by receiving an electron, while an –O group is stabilized by receiving two electrons. The electronic structures of pristine and functionalized MXenes were investigated to understand the mechanism of being semiconducting after the surface functionalization.[130] From Fig. 7b and c, there is a tiny band gap between the p and d bands of X elements. Particularly, O terminations caused large downward shifting of the Fermi level energy resulting in the synthesis of the Ti_2CO_2 semiconductor, while F functionalization led to small downward shifting. These mechanisms are supported by DOS analysis (see Fig. 7).

3.2. Magnetic properties

The application of 2D materials in spintronics has been limited because 2D materials are mostly nonmagnetic.[138] Hence, many studies have recently been carried out to improve the magnetic properties of MXenes. Fortunately, several MXenes such as Mn_2C, Cr_2N, Cr_2C, Ti_2N, and Ti_2C are inherently magnetic. It has been found that Mn_2C[139] and Cr_2N[140] are antiferromagnetic, but

Cr_2C,[141] Ti_2N,[142] and Ti_2C[140] are ferromagnetic. Recently, magnetic MXenes with half-metallic features have been studied, where one spin-channel is semiconducting, while the other one is metallic; thereby resulting in entirely spin-polarized electrons at the Fermi level.[138] The band structure of Cr_2C (a half-metallic MXene) is presented in Fig. 8a, which shows an insulating spin-down channel and a metallic spin-up channel.[141]

Surface modification can also affect the magnetic properties of MXenes. It can lead to a surface-functionalized MXene with poorer magnetic properties, which are induced by unpaired surface electrons of transition metal elements.[138] For instance, modification with –Cl, –OH, –H, and –F groups changes the ferromagnetic half metal of pristine Cr_2C to an antiferromagnetic semiconductor.[143] However, modification with –O groups endows Cr_2NO_2 MXene with a ferromagnetic half metal feature.[140] Furthermore, Mn_2CCl_2 MXene displays an antiferromagnetic insulator characteristic, while the pristine Mn_2C is an antiferromagnetic metal. Interestingly, a ferromagnetic half metal of Mn_2CF_2 with a sizeable and half metallic gap, and a high Curie temperature, was fabricated.[144] Moreover, as reported by Khazaei et al., functionalized Cr_2N and Cr_2C MXenes
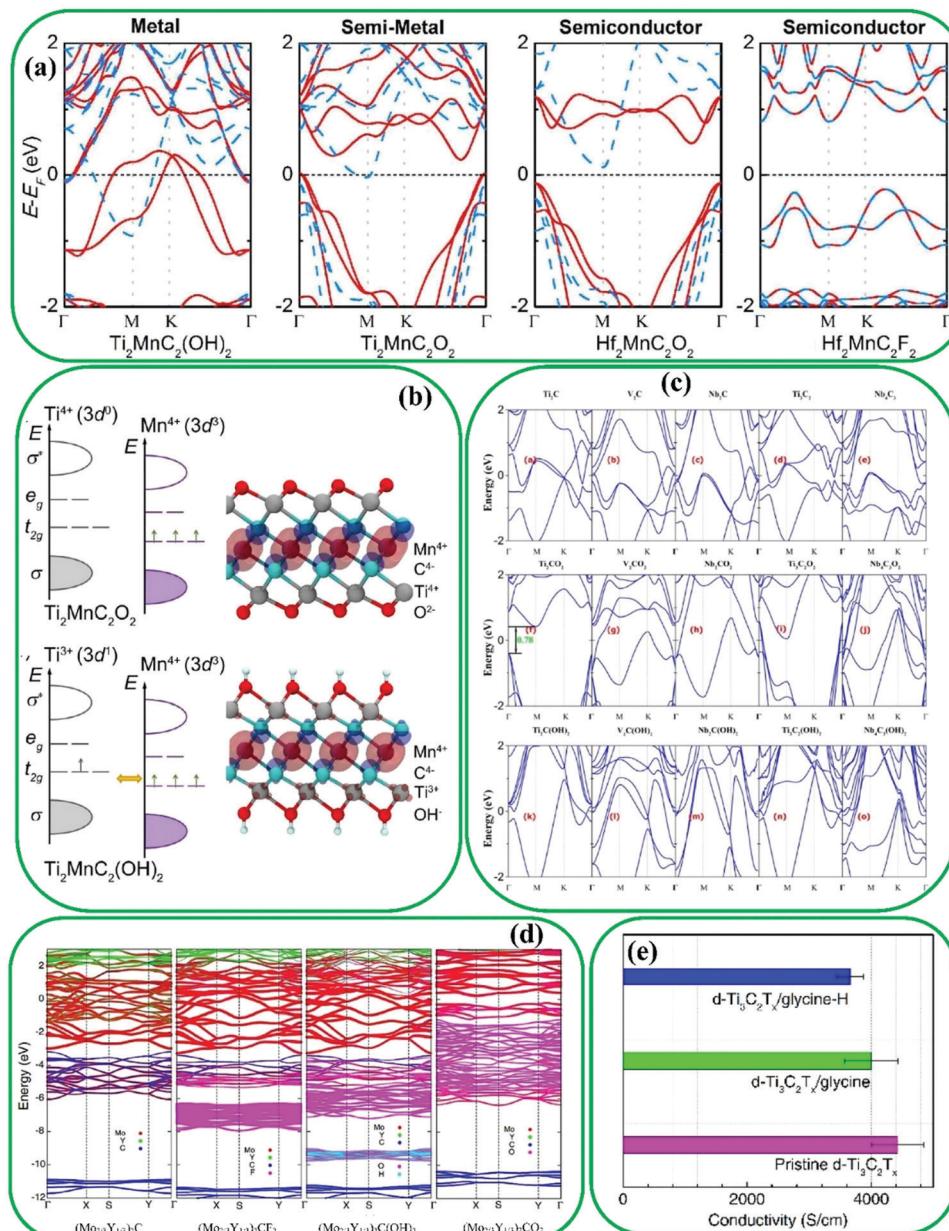
Fig. 6 (a) Electronic band structures of different MXenes showing the effect of termination groups and transition metal elements on the MXene properties, (b) electronic band structures around the Fermi level (E_F) for Ti$_2$MnC$_2$O$_2$ and Ti$_2$MnC$_2$(OH)$_2$. Reproduced with permission.[132] Copyright 2017, American Chemical Society. (c) Electronic band structures of pristine MXenes (M$_n$C$_{n-1}$), O- and OH-terminated MXenes, where the Fermi level is zero. Reproduced with permission.[133] Copyright 2017, American Chemical Society. (d) Electronic band structures of pristine (Mo$_{2/3}$Y$_{1/3}$)$_2$C and the corresponding surface terminated MXenes. Reproduced with permission.[135] Copyright 2018, American Physical Society. (e) The comparison of electrical conductivity between pristine Ti$_3$C$_2$ and Ti$_3$C$_2$/glycine hybrid. Reproduced with permission.[54] Copyright 2018, The Royal Society of Chemistry.

are ferromagnetic,[130] and this could be related to the d orbitals of Cr, as it has been theoretically indicated that Cr atoms might have magnetic moments of (0.45μ_B/Cl) in MAX phases.[145]

The magnetic properties of functionalized MXenes with asymmetrical functionalization groups have been widely evaluated. As reported, Cr$_2$CFOH, Cr$_2$CHF, Cr$_2$CHCl, Cr$_2$CClBr, and Cr$_2$CFCl are antiferromagnetic semiconductors with a Néel temperature of almost 400 K.[144] Ferromagnetic or antiferromagnetic properties of asymmetrical functionalized Cr$_2$C MXenes are similar to symmetrical functionalized materials.[144]

Fig. 8b shows the DOS of Cr$_2$CFCl and Cr$_2$CF$_2$, where Cr$_2$CFCl exhibited bipolar magnetic semiconductor characteristics, indicating that the valence band maximum and the conductive band minimum show opposite spin polarization in comparison to Cr$_2$CF$_2$ with symmetrical functionalization groups.

3.3. Mechanical properties

Surface terminations of MXenes are considered as a main factor for their mechanical properties.[146] Generally, O-terminated MXenes show higher stiffness compared to –OH and –F
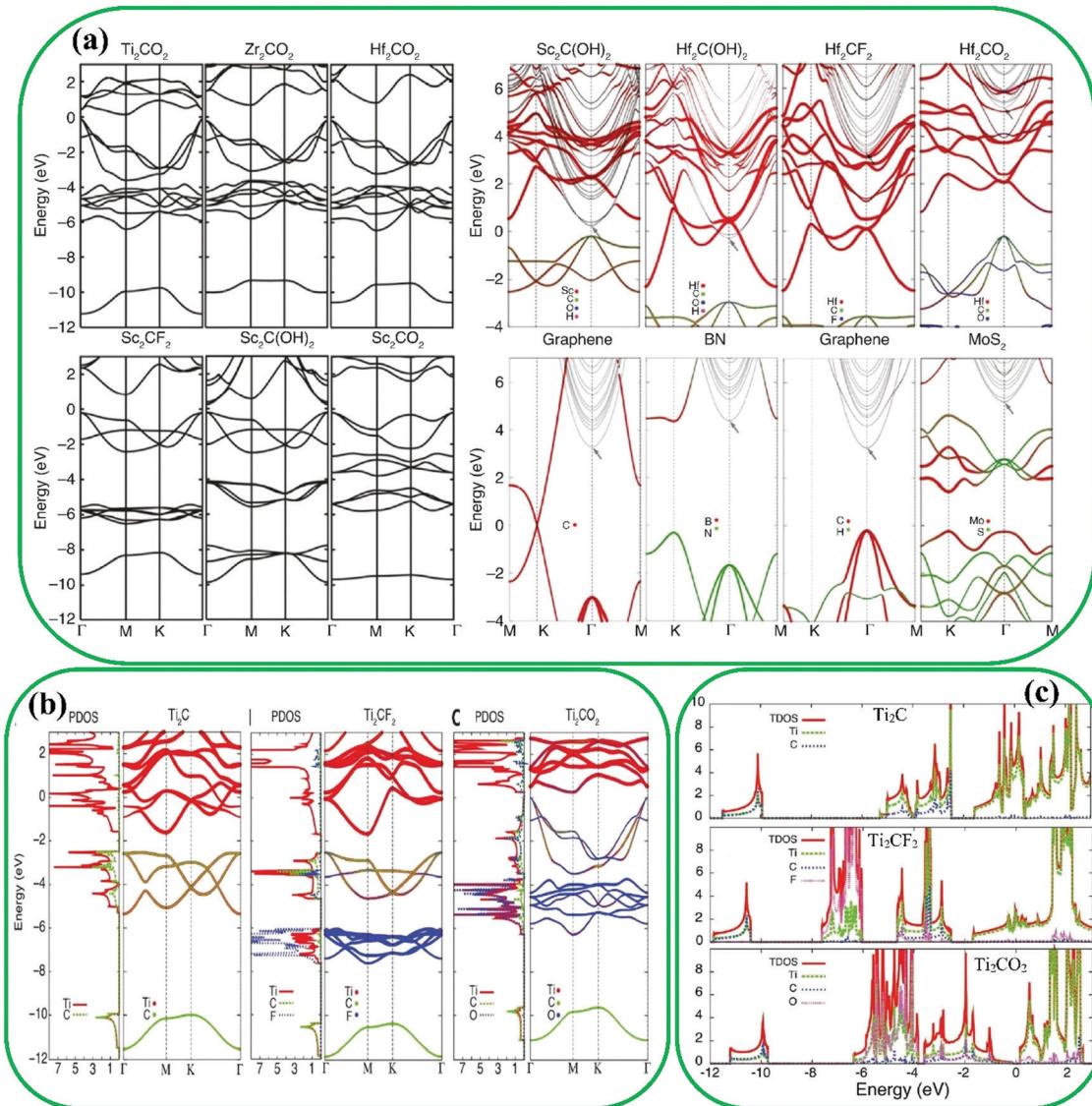
Fig. 7 (a) Band structures of M_2CT_2 MXenes, showing the effect of T termination groups and M elements on the band structure and also their projected band structures. Reproduced with permission.[130] Copyright 2013, Wiley. (b) Projected DOSs and band structures of pristine Ti_2C, Ti_2CF_2, and Ti_2CO_2. Reproduced with permission.[137] Copyright 2017, The Royal Society of Chemistry. (c) The DOS for pristine Ti_2C, and F- and O-terminated MXenes. Reproduced with permission.[130] Copyright 2013, Wiley.

terminated MXenes.[147] This phenomenon can be attributed to the various lattice properties of MXenes with diverse termination groups.[148] For example, Guo *et al.* reported that the surface functionalization of Ti_2C leads to increased flexibility,[149] increased strain, but decreased Young's modulus.[149] The critical strain increases, and the collapse of Ti layers decelerates, because the different functional groups on the surface of MXenes act as a delimiter under tensile deformation.

Another factor that influences the mechanical properties is the number of atomic layers of MXenes based on their chemical formula. In this regard, Borysiuk *et al.* found that the hardness and tensile strength of an $M_{n+1}X_n$ MXene increase with decreased n.[150] Furthermore, the mechanical properties of MXenes can be improved by incorporating CNTs and polymerizing with various types of polymers.[146] It has been reported that

MXene–polymer composites have higher compressive and tensile strengths, toughness, and flexibility, compared to pristine MXenes. For instance, the Ti_3C_2/PVA composite exhibited larger tensile strength compared to pristine Ti_3C_2.[146] Additionally, Ti_3C_2/ultrahigh molecular weight polyethylene (UHMWPE)[151] and Ti_3C_2/polyacrylamide (PAM)[152] composites have higher yield strength and toughness compared to pristine Ti_3C_2.

3.4. Optical properties

Optical properties of MXenes, including refractive index, reflectivity, absorption, and transmittance are of importance in different applications. There have been a few experimental studies on the effect of surface functionalization on optical properties.[153,154] For instance, pristine Ti_3C_2 showed 77% transmittance in visible light, while the 30% transmittance
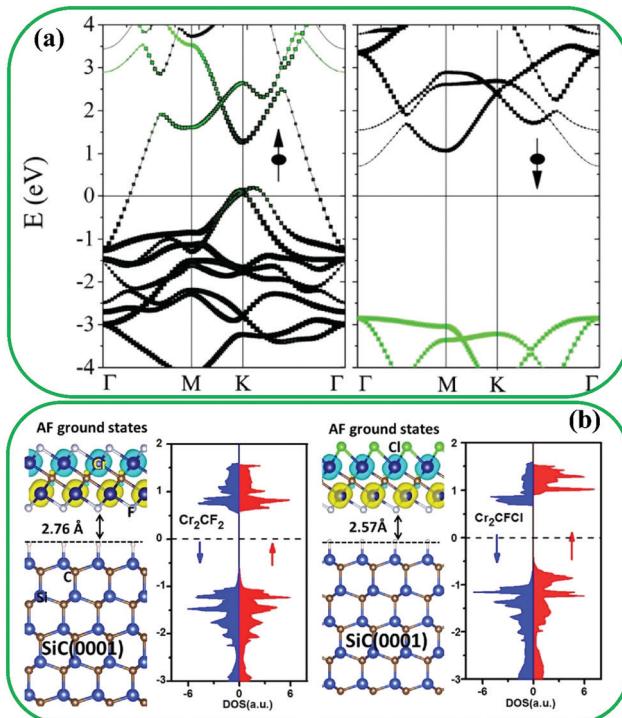
Fig. 8 (a) Band structure of pristine Cr_2C MXene. Reproduced with permission.[141] Copyright 2015, American Chemical Society. (b) DOS of Cr_2CFCl asymmetrically functionalized and Cr_2CF_2 symmetrically functionalized. Reproduced with permission.[144] Copyright 2016, The Royal Society of Chemistry.

was observed for a thin Ti_3AlC_2 MAX phase.[155,156] Ammonium bifluoride (NH_4HF_2) intercalated Ti_3C_2 thin films ($Ti_3C_{2.3}$-$O_{1.2}F_{0.7}N_{0.2}$) showed 90% transmittance.[156] Optical properties such as reflection, absorption, and transmittance can be investigated theoretically by calculating the imaginary part of the dielectric function tensor at different photon wavelengths.[147,157] Bai *et al.* reported the optical properties of pristine Ti_2C and

functionalized Ti_2C with –O, –OH, and –F in both out-plane and in-plane directions (Fig. 9a). It can be seen obviously that the in-plane absorption coefficients of OH- and F-functionalized Ti_2C MXenes are lower in comparison to pristine and O-functionalized Ti_2C MXenes. Moreover, the white color indicates the OH- and F-functionalized Ti_2C according to the refractivity results. Furthermore, the performance of MXenes in visible and UV light absorption is the key factor for the optoelectronic, photovoltaic, and photocatalytic properties, which are affected by the existence of functional groups (Fig. 9b).[75,158,159] The same properties were observed for F- and OH-functionalized MXenes, in contrast to the performance of O-functionalized MXenes. Additionally, in the UV range, the reflectivity improved in comparison with pristine MXenes, while in the visible region, the F- and OH-functionalized MXenes decreased the reflectivity and absorption (Fig. 9c).

3.5. Hydrophilicity/hydrophobicity

As mentioned earlier, MXenes have shown superior performance in numerous applications.[160–163] However, MXenes degrade in the presence of water and oxygen because of their hydrophilic nature induced by –O, –F, and –OH functional groups.[164–168] The surface functionalization of MXenes has been reported as an efficient strategy to enhance their stability as well as their surface characteristics.[169] For example, Ji *et al.* functionalized Ti_3C_2 with silylation reagents ((3-aminopropyl)-triethoxysilane (APTES)) to tune its hydrophilicity (Fig. 10a).[170] The stability of Ti_3C_2 improved by APTES functionalization by blocking the contact between water and MXenes. This improvement was also achieved for hexadecyltrimethoxysilane and $1H,1H,2H,2H$-perfluorodecyltriethoxysilane (FOTS) (Fig. 10b). The results indicated the change of surface properties from hydrophilic to hydrophobic. Two superhydrophobic self-assembled monolayers (SAMs) [(3-chloropropyl)trimethoxysilane (CPTMS) and FOTS] were used for surface modification of MXenes *via* formation of covalent bonds between –OH and different surface functional groups (Fig. 10c).[171,172] The water contact angle results (Fig. 10d)
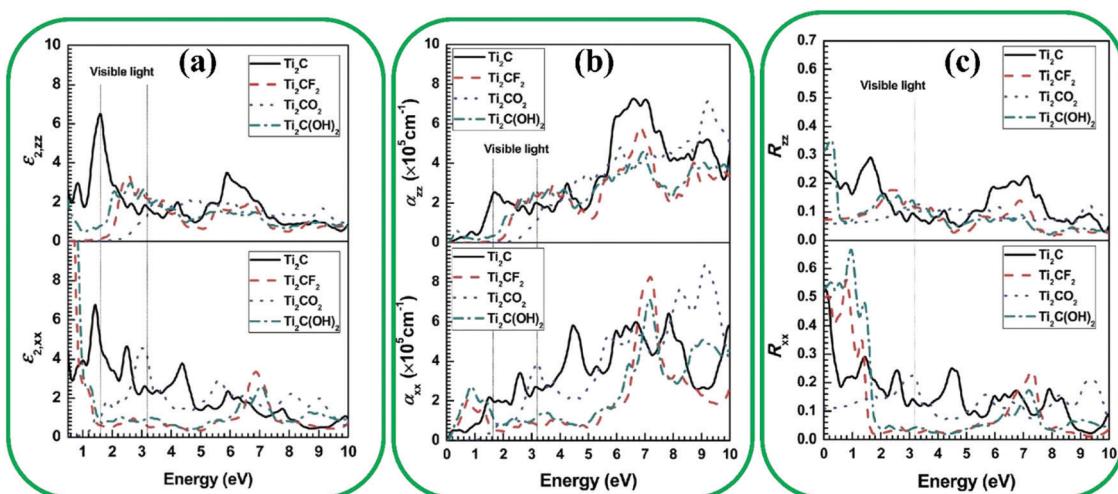
Fig. 9 (a) Imaginary part (ε_2), (b) adsorption coefficient (α), and (c) reflectivity (R) in the in-plane (XX) and out-plane (ZZ) as a function of photon frequency for surface-modified Ti_2CT_2 MXenes. Reproduced with permission.[147] Copyright 2016, The Royal Society of Chemistry.
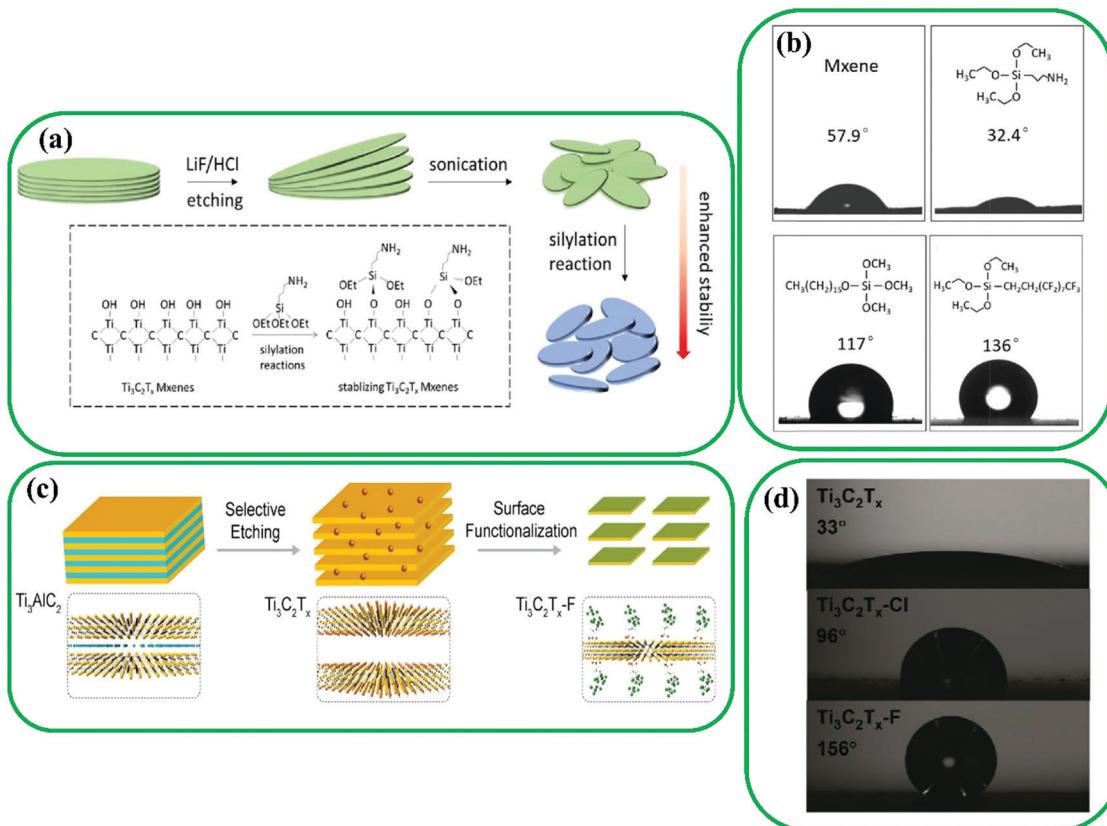
Fig. 10 (a) Schematic representation of surface functionalization of Ti_3C_2 with silylation agents. (b) Water contact angle of various surface-modified Ti_3C_2. Reproduced with permission.[170] Copyright 2019, Elsevier. (c) Modification process of Ti_3C_2 flakes. (d) Water contact measurements for pristine Ti_3C_2, Ti_3C_2-Cl, and Ti_3C_2-F. Reproduced with permission.[173] Copyright 2020, American Chemical Society.

showed a superhydrophobicity of $156°$ and $96°$ for the fluorine-containing (Ti_3C_2-F) and chlorine-containing (Ti_3C_2-Cl) films, respectively, while the pristine Ti_3C_2 is basically hydrophilic due to its –O and –OH functional groups (a water contact angle of $33°$). Hence, the functionalization of Ti_3C_2 with superhydrophobic reagents such as FOTS and CPTMS can be an effective approach to inhibit the degradation of MXene materials.

4. Applications

Because of their synergistic properties, functionalized MXenes have shown significantly better performances in comparison to pristine MXenes.[6,174–177] To understand the effect of a specific functionalization on a MXene, the structural and application-specific properties of functionalized MXenes should be studied. To this end, herein, applications of surface-modified MXenes in fields such as biomedical application, sensors, catalysis, energy storage and conversion, and membrane-based separation are reviewed.

4.1. Biomedical applications

MXenes have been extensively used in biomedical applications owing to their outstanding properties such as magnetic, electronic, optical, etc. MXenes are typically non-toxic and biocompatible

due to multiple compositions.[42] The different functional groups (–F, –O, and –OH) on the surface of MXenes make them hydrophilic. Moreover, MXenes have excellent light absorption in the near-infrared (NIR) region, which allows their use in photoacoustic imaging (PAI) and photothermal therapy (PTT) applications.[52] Additionally, the surface of MXenes can be easily modified by various approaches, providing new opportunities for further biomedical applications.[36,99,178–180]

4.1.1. Photoacoustic imaging. Lin *et al.* reported that modified Ti_3C_2 MXenes with SP possesses enhanced the physiological stability, compared to pristine Ti_3C_2.[35] The UV-vis-NIR absorption spectra of Ti_3C_2 demonstrated an absorption of around 750–850 nm at $\lambda = 808$ nm, and the absorption intensity remarkably increased by increasing the concentration of Ti_3C_2 (Fig. 11a). An extinction coefficient of 25.2 L g^{-1} cm^{-1} was achieved, and a linear relationship between the Ti_3C_2 concentration and the normalized adsorption intensity was observed. The photothermal performance of Ti_3C_2 was measured at various C concentrations at a power density of 1.5 W cm^{-2} (Fig. 11b), where the temperature of the solution (containing 72 ppm Ti_3C_2 MXenes) reached 57 °C, while the temperature of clean water had not changed, indicating the fast conversion of NIR light to thermal energy. Furthermore, the efficient effect of Ti_3C_2-SP MXene on the photothermal properties was confirmed under NIR laser irradiation, where by increasing the
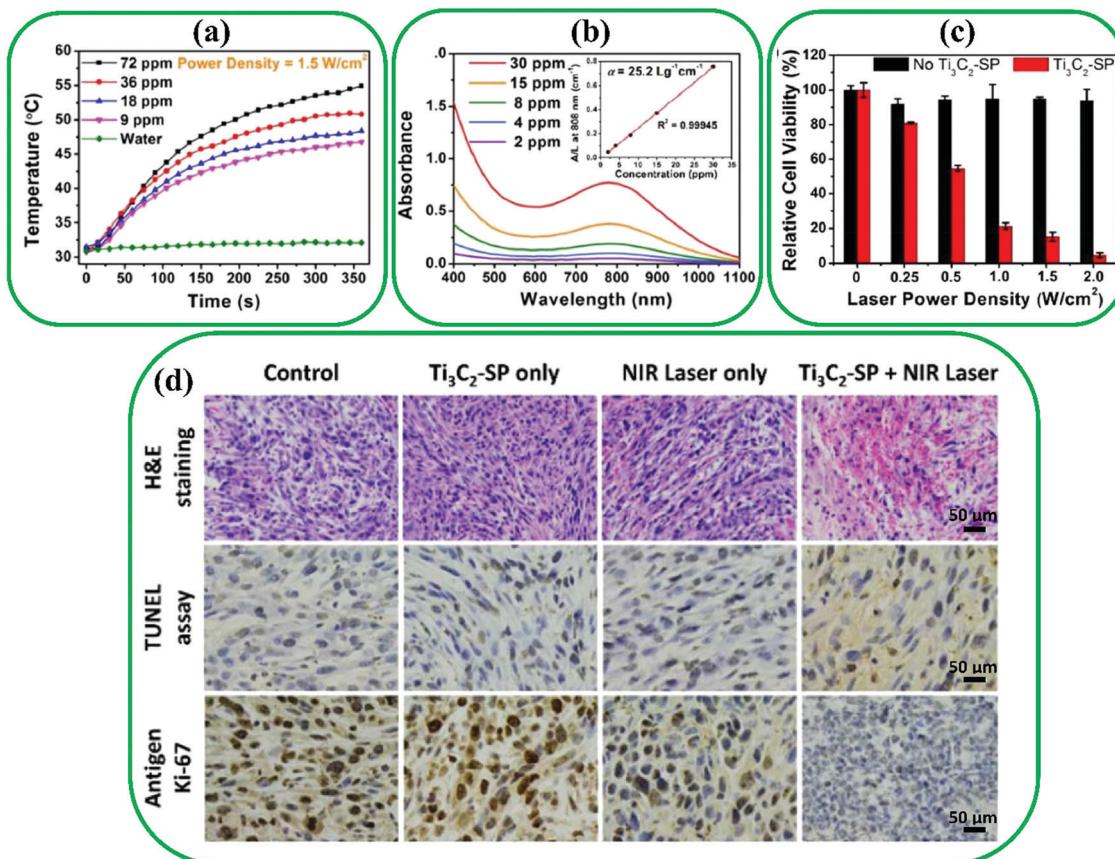
Fig. 11 (a) Photothermal heating measurements of water and suspended Ti_3C_2 in water under a laser irradiation power of 1.5 W cm^{-2}. (b) Absorbance spectra of suspended Ti_3C_2 in water at different concentrations. Inset: Normalized absorbance intensity at $\lambda = 808$ nm. (c) Relative cell viability of Ti_3C_2-SP at various laser power densities. (d) H&E, TUNEL, and antigen Ki-67 immunofluorescence staining for pathological changes *in vivo*, apoptosis in tumor, and cellular proliferation in tumor, respectively. Reproduced with permission.[35] Copyright 2017, American Chemical Society.

power density, more cells incubated with SP-modified Ti_3C_2 were killed compared to cells without Ti_3C_2-SP. TdT-mediated dUTP Nick-End labeling (TUNEL) and hematoxylin and eosin (H&E) staining indicated more necrosis of tumor cells after treatment with Ti_3C_2-SP under NIR laser irradiation than after treatment with other materials (Fig. 11c). Fig. 11d shows the strong effect of Ti_3C_2-SP under NIR laser irradiation on the *in vivo* proliferative activity of the Ki-67 antibody.

4.1.2. Biosensing. In addition, surface-functionalized MXenes have received a lot of attention in biosensing because of their outstanding biocompatibility, excellent electrical properties, and large surface area.[181] For example, a new organ-like MXene-based material was prepared for biosensing applications to detect H_2O_2 in the range of 0.1–260 μM.[182] Hereby, hemoglobin (Hb), as a protein, was utilized for the modification of the surface of Ti_3C_2 MXenes (Fig. 12a). The cyclic voltammogram (CVs) performances of Hb-functionalized Ti_3C_2 electrodes under the physiological condition of pH 7.0 are shown in Fig. 12b, where the Nafion/MXenes/glassy carbon (GC) electrode (curve a) did not show any redox peak, demonstrating its electro-inactive state in the potential window. Besides, two redox peaks can be observed at -0.327 V and -0.367 V *vs.* Ag/AgCl for the Nafion/Hb/MXenes/GC electrode

(curve b), indicating that an appropriate microenvironment can be achieved for Hb to facilitate the reaction of electron transfer. A smaller redox peak is seen at the Nafion/Hb/GC electrode (curve c), which may be attributed to the unsuitable direct electron transfer (DET) between the electrode and the enzyme. It can be concluded that the DET process between the GC electrode and Hb molecules improved at the Nafion/Hb/MXene/GC electrode. Moreover, the Nafion/Hb/MXene/GC electrode exhibited good performance in detecting H_2O_2 by the measurement of amperometric responses (Fig. 12c and d). The nitrite biosensor and glucose biosensor based on MXenes have been reported in the literature.[183,184] Hence, MXene-based materials have shown incredible potential for enzyme conjugation and biosensing applications.

4.1.3. Photothermal therapy and drug delivery system. Cancer disease is a major cause of death worldwide.[185] Recently, many operation treatments have been developed for cancer therapy, although most of them, such as radiotherapy and chemotherapy, not only do not remove cancer tumors completely, but also create side effects.[186] Therefore, photothermal therapy (PTT) has emerged as a highly efficient strategy to prevent the growth of cancer tumors because PTT can transform NIR light to thermal energy.[187] It should be noted
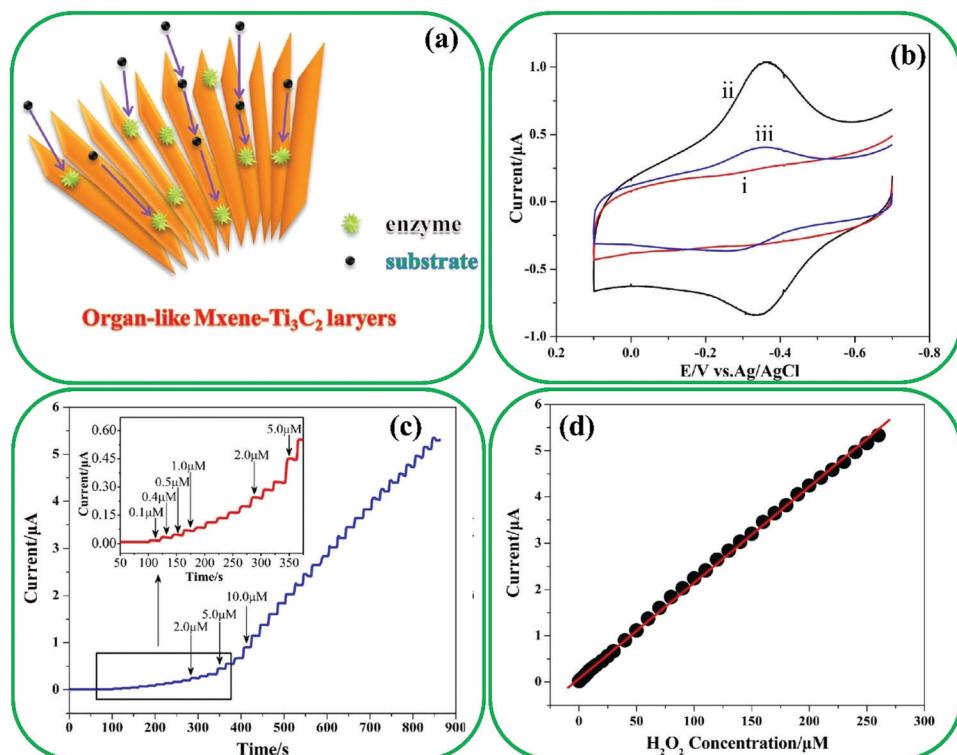
Fig. 12 (a) Schematic presentation of organ-like Ti_3C_2 encapsulating hemoglobin. (b) Cyclic voltammograms with a scan rate of 0.1 V S^{-1} in 0.1 M of (i) Nafion/Ti_3C_2/GC electrode, (ii) Nafion/Hb/Ti_3C_2/GC electrode, and (iii) Nafion/Hb/GC electrode. (c) The current time response of the Nafion/Hb/Ti_3C_2/GC electrode to the addition of H_2O_2 under stirring conditions. (d) The steady state as a function of H_2O_2 concentration. Reproduced with permission.[182] Copyright 2014, IOP Science.

that NIR light is classified into two sections, including first bio-window (750–1000 nm) and second bio-window (1000–1350 nm), where a few studies have utilized the second bio-window in PTT applications because there are no adequate materials with high-efficient photothermal conversion and tailored NIR light absorption.[188] Interestingly, MXene-based materials have attracted tremendous attention for PTT applications owing to their high photothermal conversion and strong absorption. For instance, Lin *et al.* prepared poly(vinylpryrrolidone) (PVP)-functionalized Nb_2C MXenes for using in the PTT of mice tumor xenografts, as depicted in Fig. 13a and b.[99] At first glance, other treatment methods were applied on the tumor cells of mice, while the tumor cells are still large (Fig. 13c). Fig. 13d and e indicate that tumor regions entirely vanished once PTT was used by Nb_2C-PVP + NIR-I and Nb_2C-PVP + NIR-II. Fig. 13f depicts the comparison of survival curves for various treatment techniques, where it can be clearly seen that the recovered mice by Nb_2C-PVP + NIR-I and Nb_2C-PVP + NIR-II survived for more than 50 days.

MXene-based materials provide numerous opportunities to be anchored by therapeutic molecules, so they are widely applied for developing drug delivery systems.[189] Recently, Han *et al.* synthesized Ti_3C_2 immobilized by SP for drug delivery of PTT and chemotherapy (Fig. 14a and b),[37] which led to facile transport in blood vessels and superior water dispersibility.[190] Afterward, electrostatic adsorption was used

for the conjugation of anti-cancer drugs (Dox and doxorubicin) on the surface of Ti_3C_2-SP MXenes. The results showed that the photothermal conversion of Ti_3C_2-SP MXene led to a noticeable improvement of Dox release under laser irradiation. The red fluorescence (Fig. 14c–e) demonstrated more dead cells by combining laser irradiation and Dox@Ti_3C_2-SP MXenes compared with other groups (Ti_3C_2-SP + laser and Dox@Ti_3C_2-SP).

4.2. Sensors

MXenes have been found to have promising potential in sensing applications, such as electrochemical sensors,[33] strain sensors,[191–193] biosensors,[194–196] and gas sensors,[31,197] due to their piezoelectric and thermoelectric response, rich surface groups, large surface area, and excellent anisotropy of conductivity. For instance, Shi *et al.* prepared layered Ti_3C_2–Ag nanowire-PDA/Ni^{2+} nanocomposite film-based strain sensors using a microscale "brick-and-mortar" architecture.[192] They incorporated either Ni^{2+} or PDA into Ti_3C_2–Ag nanowires. As shown in Fig. 15a, the Ti_3C_2–Ag nanowire-PDA/Ni^{2+} nanocomposite exhibited superior performance of 83% stretchability compared to those of the pristine Ti_3C_2–Ag nanowire (32%), Ti_3C_2–Ag nanowire-Ni^{2+} (47%), and Ti_3C_2–Ag nanowire-PDA (75%). The output signals of Ti_3C_2–Ag nanowire-PDA/Ni^{2+} sensors were measured at various strains (Fig. 15b), and at a strain of 80%, the steady electrical responses of the sensors resulted in a strain rate of 1.2–8 mm S^{-1}. Furthermore, the practical potential
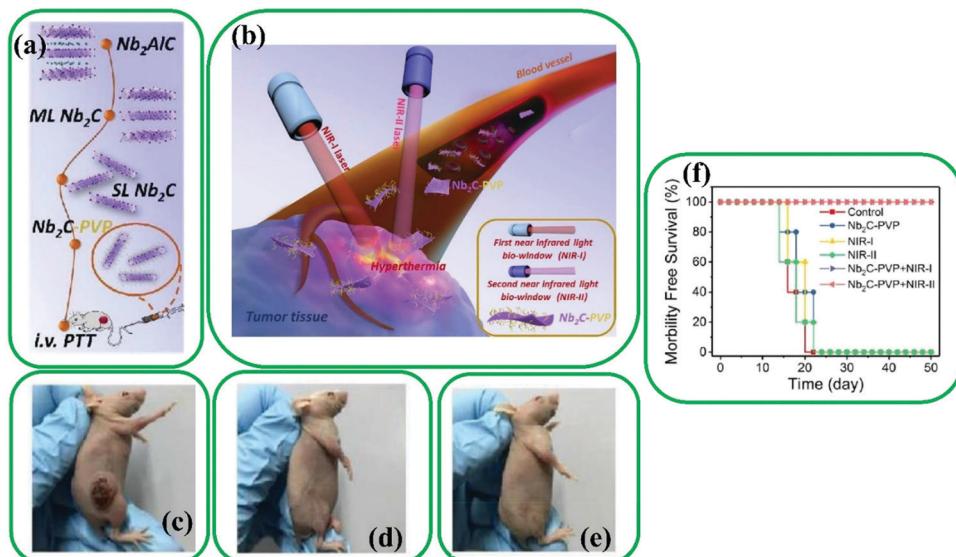
Fig. 13 (a) and (b) Exhibition of surface functionalization of Nb_2C with PVP for *in vivo* photothermal tumor ablation in NIR-I and NIR-II biowindows. (c)-(e) Images of tumor regions of mice after 16 days of different treatments; (c) control, (d) Nb_2C-PVP + NIR-I, and (e) Nb_2C-PVP + NIR-II. (f) Survival curves of mice after different treatments. Reproduced with permission.[99] Copyright 2017, American Chemical Society.
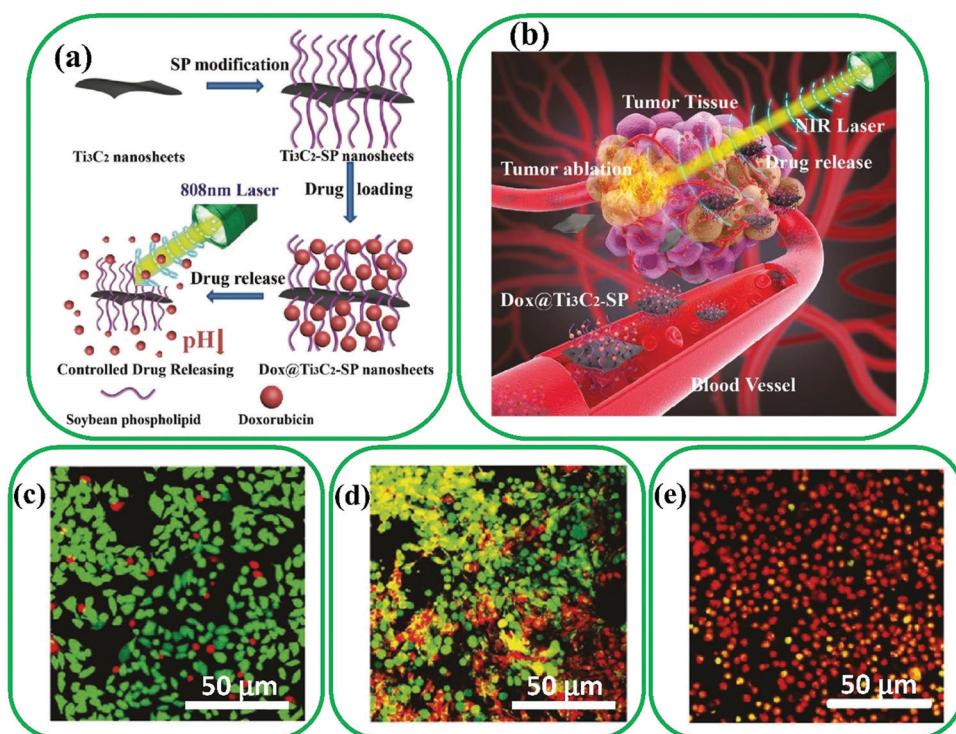
Fig. 14 (a) Schematic illustration of Ti_3C_2 surface functionalization by SP, drug loading on the surface of the modified Ti_3C_2 MXenes, and stimuli-responsive drug release by inner and external irradiation. (b) Drug delivery scheme of surface-modified Ti_3C_2 *in vivo* synergistic photothermal and chemotherapy of cancer, including transport in blood vessels, accumulation in tumor, drug release, and NIR laser ablation of tumor. CLSM images of cells after the treatment with (c) Dox@Ti_3C_2-SP, (d) Ti_3C_2-SP + laser, and (e) Dox@Ti_3C_2-SP + laser. The green and red fluorescence represent the live and dead cells, respectively. Reproduced with permission.[37] Copyright 2018, Wiley.

of the Ti_3C_2–Ag nanowire-PDA/Ni^{2+} strain sensor was verified by the attachment of two individual strain sensors on the skin of the knee and wrist joint of a volunteer (Fig. 15c). Fig. 15d shows

the electrical signals generated by the strain sensor on the wrist when the volunteer is walking. The radial waves of a single heartbeat, including percussion (P), tidal (T), and diastolic (D),
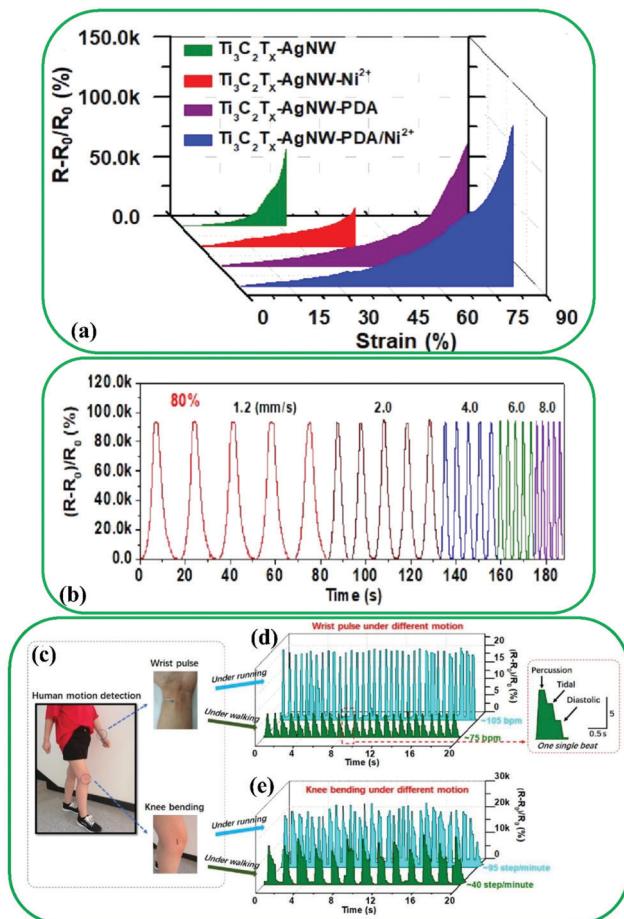
Fig. 15 (a) Typical relative resistance change *vs.* applied strain for the Ti$_3$C$_2$–AgNW, Ti$_3$C$_2$–AgNW–PDA, Ti$_3$C$_2$–AgNW–Ni^{2+}, Ti$_3$C$_2$–AgNW–PDA/Ni^2 sensors. (b) Relative resistance variation of the Ti$_3$C$_2$–AgNW–PDA/Ni^{2+} strain sensor under incremental strain rates cycling from 0 to 80%. Monitoring human body (knee bonding and wrist pulse) under running and walking conditions by means of Ti$_3$C$_2$–AgNW–PDA/Ni^{2+} strain sensors. (c) Images of wearable strain sensors attached to the wrist and knee. (d) Relative resistance variation of a wrist pulse. (e) Relative resistance change of knee bending. Reproduced with permission.[192] Copyright 2018, American Chemical Society.

were isolated. The strain sensor detected motion signals in running, demonstrating the durability and reliability of the sensors (Fig. 15e).

Kumar *et al.* reported a biofunctionalized Ti$_3$C$_2$ (f-Ti$_3$C$_2$) *via* APTES for the detection of cancer.[90] Besides, the deposition of TiO$_2$ nanoparticles on the surface of MXenes may offer further advantages for the detection of H$_2$O$_2$.[198] Therefore, the shielding microenvironment for increasing the stability and activity of enzymes can be achieved by loading TiO$_2$ with exceptional biocompatibility on the surface of MXenes. The active sites of enzyme adsorption significantly increased for TiO$_2$–Ti$_3$C$_2$ compared with pristine Ti$_3$C$_2$. Moreover, Chen *et al.* reported that the dispersion of MXenes could be adjusted by varying the temperature and CO$_2$ concentration, which changes the conductivity and transmittance of V$_2$C,[98] where PDMAEMA was used to modify the surface of V$_2$C by self-initiated

photografting and photopolymerization. By increasing the temperature of the solution above the lower critical solution temperature (LCST), the hydrophilic nature of PDMAEMA changes to hydrophobic, resulting in the enhancement of the transmittance of V$_2$C@PDMAEMA. Besides, when CO$_2$ was added to water to form charged ammonium bicarbonate, the conductivity of V$_2$C@PDMAEMA increased because of the CO$_2$ responsive characteristic of V$_2$C@PDMAEMA, demonstrating that V$_2$C@PDMAEMA is sensitive to CO$_2$ and temperature.

4.3. Catalysis

Recently, the utilization of MXene-based materials in catalysis applications has received considerable attention. This is due to the appealing properties of MXenes such as (i) the abundant active sites and rich surface groups, (ii) the adjustable band gap of MXenes by the arrangement of surface chemistries, and (iii) the exceptional carrier mobility of MXene-based materials, which can lead to improving the migration and separation of photogenerated electron–hole pairs.[161,199,200] For example, Ramalingam *et al.* reported the coordination interactions between Ti$_3$C$_2$ and ruthenium single atoms (Ru$_{SA}$) through the S and N heteroatom doping method.[201] The polarization curves of the hydrogen evolution reaction (HER) of MXene-based materials (including Ru$_{SA}$-N-S-Ti$_3$C$_2$, Ru$_{SA}$-Ti$_3$C$_2$, N-S-Ti$_3$C$_2$, Ti$_3$C$_2$, and carbon paper) (Fig. 16a) revealed that Ru$_{SA}$, N, and S co-doped Ti$_3$C$_2$ have great potential for electrocatalytic HER performance; they showed approximately remarkable zero onset potential and the smallest overpotential of 76 and 237 mV to reach 10 and 100 mA cm^{-2}, respectively. The HER baseline of Ru$_{SA}$-doped Ti$_3$C$_2$ and Ru$_{SA}$, N, and S co-doped Ti$_3$C$_2$ catalysts are not at zero potential; this may be due to the underpotential hydrogen adsorption effect of Ru and the capacitance effect of the nanocarbons of Ti$_3$C$_2$ MXenes.[202] The slope of Tafel plots was calculated to evaluate the reaction kinetics of the catalysts in the HER process (Fig. 16b), where this slope for the Ru$_{SA}$, N, and S co-doped Ti$_3$C$_2$ catalysts was about 90 mV dec^{-1}, demonstrating that the Volmer–Heyrovsky mechanism is followed by these electrocatalysts which includes two steps: (i) fast initial discharge reaction (reaction (I)) and (ii) slow electrochemical desorption reaction (reaction (II)).[203,204]

$$H_3O^+ + e^- \rightarrow H_{ads} + H_2O \qquad (I)$$

$$H_{ads} + H_3O^+ + e^- \rightarrow H_{ads} + H_2O \qquad (II)$$
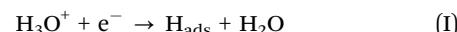
Additionally, the significant activity of the Ru$_{SA}$, N, and S co-doped Ti$_3$C$_2$ electrocatalysts was confirmed by the measurements of turnover frequency (ToF), showing the exceptional performance of these electrocatalysts compared to other Ru$_{SA}$-based electrocatalysts.

Interfacial engineering of MXene-based materials can be easily coupled with other nano-materials by the combination of large exposed basal plane and good flexibility of two phases, resulting in the formation of highly active catalysts.[205] Besides, the reaction kinetics can be improved *via* the change in the electronic structure of MXenes.[205] Recently, many studies have been performed on the effect of the interfacial structure of

© 2021 The Author(s). Published by the Royal Society of Chemistry
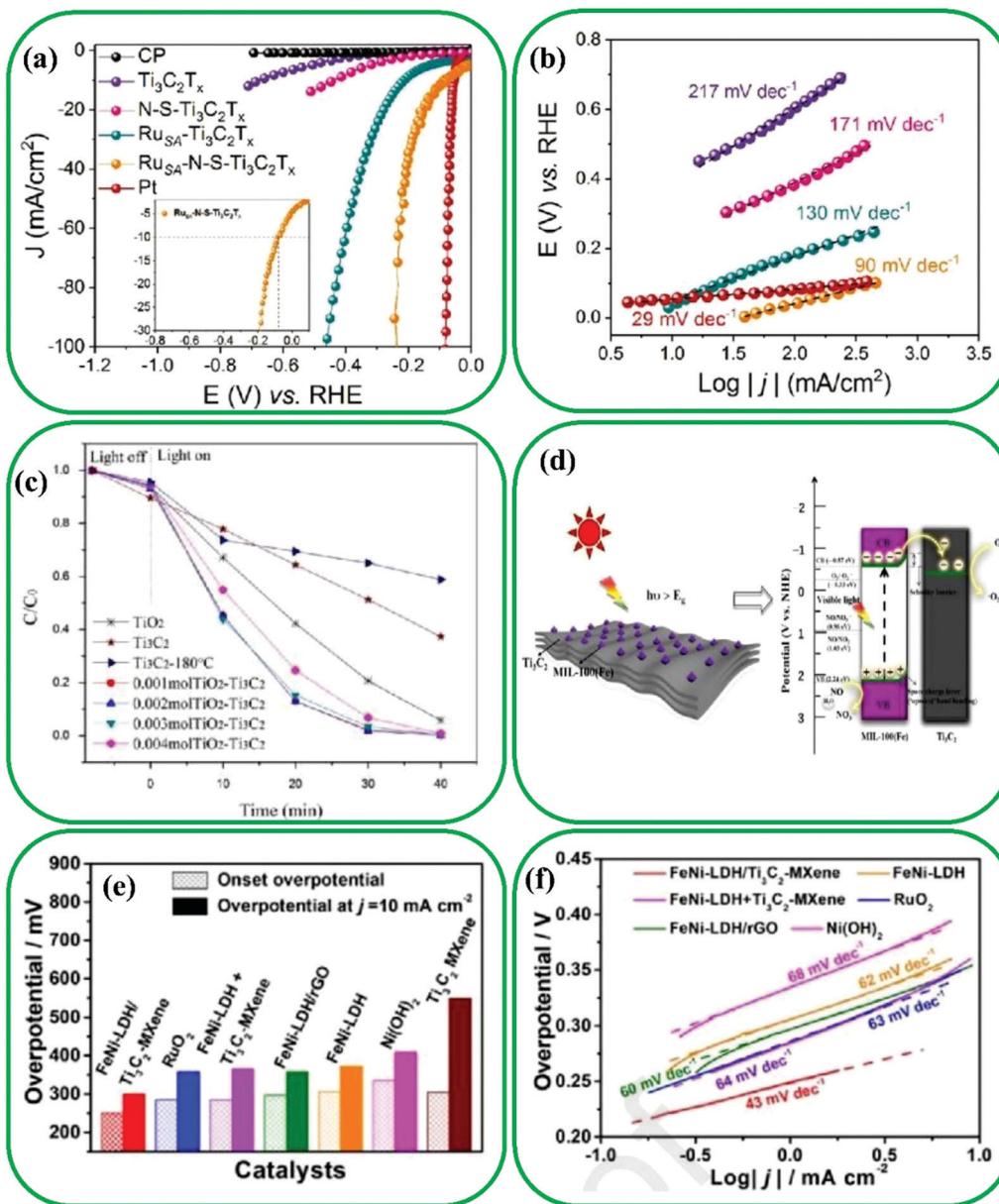
Fig. 16 Electrocatalysis HER performance of the Ru_{SA}-N-S-Ti_3C_2 catalyst. (a) The HER polarization curves in 0.5 M H_2O_2 for bare carbon paper, pristine Ti_3C_2, N-S-Ti_3C_2, Ru_{SA}-Ti_3C_2, and Ru_{SA}-N-S-Ti_3C_2 catalysts. Inset: The magnified HER polarization curve of Ru_{SA}-N-S-Ti_3C_2. (b) The Tafel plots relating to part (a). Reproduced with permission.[201] Copyright 2019, Wiley. (c) The curves of photocatalytic degradation rate for catalysts. Reproduced with permission.[208] Copyright 2015, Elsevier. (d) Proposed mechanism for photocatalytic oxidation of NO by the M/T-3 Schottky catalyst under visible light. Reproduced with permission.[210] Copyright 2019, American Chemical Society. (e) A comparison of FeNi-LDH/Ti_3C_2-MXene, RuO_2, FeNi-LDH + Ti_3C_2-MXene, FeNi-LDH/rGO, FeNi-LDH, Ni(OH)$_2$, and Ti_3C_2-MXene catalysts at overpotential and onset overpotential required to achieve a current density of 10 mA cm^2. (f) Tafel plots of the reported catalysts. Reproduced with permission.[211] Copyright 2017, Elsevier.

Ti_3C_2 MXene and TiO_2 nanoparticles on the photocatalytic reactions,[88,206,207] where the TiO_2/Ti_3C_2 was prepared by the *in situ* growth of TiO_2 on the surface of Ti_3C_2 by a hydrothermal strategy.[208] As Fig. 16c shows, the TiO_2/Ti_3C_2 exhibited superior photocatalytic degradation (almost 98%) compared to pristine TiO_2 (42%) in 30 min; this can be related to the effective electron–hole separation. In addition, a mild oxidation method has been applied for the homogeneous growth of Nb_2O_5 on the surface of Nb_2C MXenes in order for the HER.[209]

Charge carriers were generated at the interface of Nb_2O_5/Nb_2C due to the contact between conductive Nb_2O_5 and Nb_2C. Wang *et al.* formed a Schottky barrier in MIL-100(Fe)/Ti_3C_2 (Fig. 16d).[210] The efficient visible light photocatalytic properties obtained for MIL-100(Fe)/Ti_3C_2 were three and four times higher than those for pristine MIL-100 and Ti_3C_2, respectively.

Moreover, FeNi-LDH nanoplates were interfacially coupled on the surface of Ti_3C_2,[211] leading to an increase in the positive charge of FeNi-LDH/Ti_3C_2 owing to the strong electronic

junction between the Ti_3C_2 MXenes and FeNi-LDH. This indicated the significant improvement of the oxygen evolution reaction (OER) performance, as the Tafel slope decreased from 62 to 43 mV dec^{-1} in comparison to FeNi-LDH (Fig. 16e and f). The HER activity of Nb-doped Ti_3C_2 was enhanced by surface modification with an Ni/Co alloy, which led to the weakening of the M–H affinity.[212] DFT calculations showed that better catalysts can be fabricated by replacing Ti with Co or Ni, which can be attributed to the synergistic effect of Ni/Co@Nb-doped Ti_3C_2.

MXene-based materials have also found applications in photocatalytic water splitting, a novel technology of clean energy conversion.[138] Traditional catalysts such as precious metal-based oxides have shown low efficiency due to their high cost and scarcity.[213,214] However, recently MXene-based materials have been widely utilized in photocatalytic water splitting technology because of their rich exposed metal sites, suitable hydrophilicity, and excellent electronic conductivity. The OER is considered as a key reaction in water splitting because it allows the production of highly pure O_2. The high catalytic performance of MXene-based materials can be obtained by adjusting their geometric properties.[205] It was found that N-doped Ti_3C_2 (denoted as $Ti_3C_{1.6}N_{0.4}$) possessed high electrical conductivity in comparison to pristine Ti_3C_2 (Fig. 17b).[215] The smaller contact angle with the KOH electrolyte can be seen for the prepared film of $Ti_3C_{1.6}N_{0.4}$ MXene, confirming its suitability as an electrolyte for the OER (Fig. 17a). As depicted in Fig. 17c and d, the Tafel slope and onset potential of the $Ti_3C_{1.6}N_{0.4}$ film were 216.4 mV dec^{-1} and 245.8 mV, respectively, showing better electrocatalytic properties compared to the

pristine Ti_3C_2. Furthermore, the surface structures of Mo_2C were tuned by incorporating isolated cobalt atoms into the lattice of Mo_2C MXenes, leading to a lower overpotential.[216] Moreover, using an electrodeposition approach, Pt atoms were anchored on the surface of Mo_2TiC_2. The resulting material showed high HER performance, which can be ascribed to the efficient active site of Pt atoms for the HER.[217] DFT calculations exhibited strong atomic interactions in Mo_2TiC_2–Pt_{SA}, resulting in the enhancement of d-electron domination near the Fermi level and also conductivity, and consequently, leading to improved catalytic activity. Besides, the strong bonding between the Mo_2TiC_2 and Pt atoms led to improved stability properties.

4.4. Energy storage and conversion

4.4.1. Energy storage. MXene-based materials have great potential for energy storage and conversion applications, because of their appropriate mechanical stability, metallic conductivity, and good hydrophilic surface.[6,115] The low capacity and tendency of restacking of pristine MXenes have restricted their applications in energy storage and conversion, which can be overcome by surface functionalization of MXenes.[26] In the case of battery performance, the volume variation of charge and discharge cycles can be substantially diminished, while modified MXenes have exhibited improved performance.[218,219] For instance, a melamine formaldehyde template method was employed to fabricate N-doped Ti_3C_2 for lithium (Li)–sulfur (S) chemistry, as a highly efficient electrocatalyst.[220] The process of conversion and capture of lithium polysulfides (LiPSs) by porous N-doped Ti_3C_2
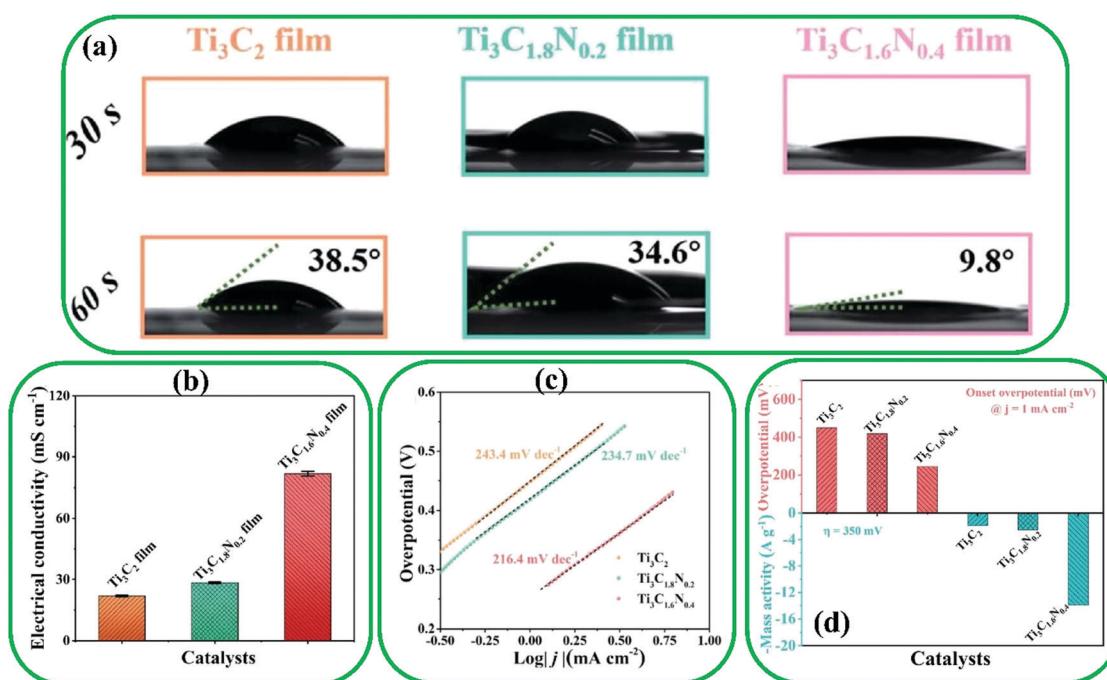

Fig. 17 (a) The contact angle measurements of Ti_3C_2, $Ti_3C_{1.8}N_{0.2}$, and $Ti_3C_{1.6}N_{0.4}$ films in a 1M KOH electrolyte. (b) Electrical conductivity of the three films. (c) Tafel plots of the three electrocatalysts. (d) Comparison of the Ti_3C_2, $Ti_3C_{1.8}N_{0.2}$, and $Ti_3C_{1.6}N_{0.4}$ electrocatalysts at an onset overpotential of 1.0 mA cm^{-2} and a mass activity of 350 mV. Reproduced with permission.[215] Copyright 2020, The Royal Society of Chemistry.
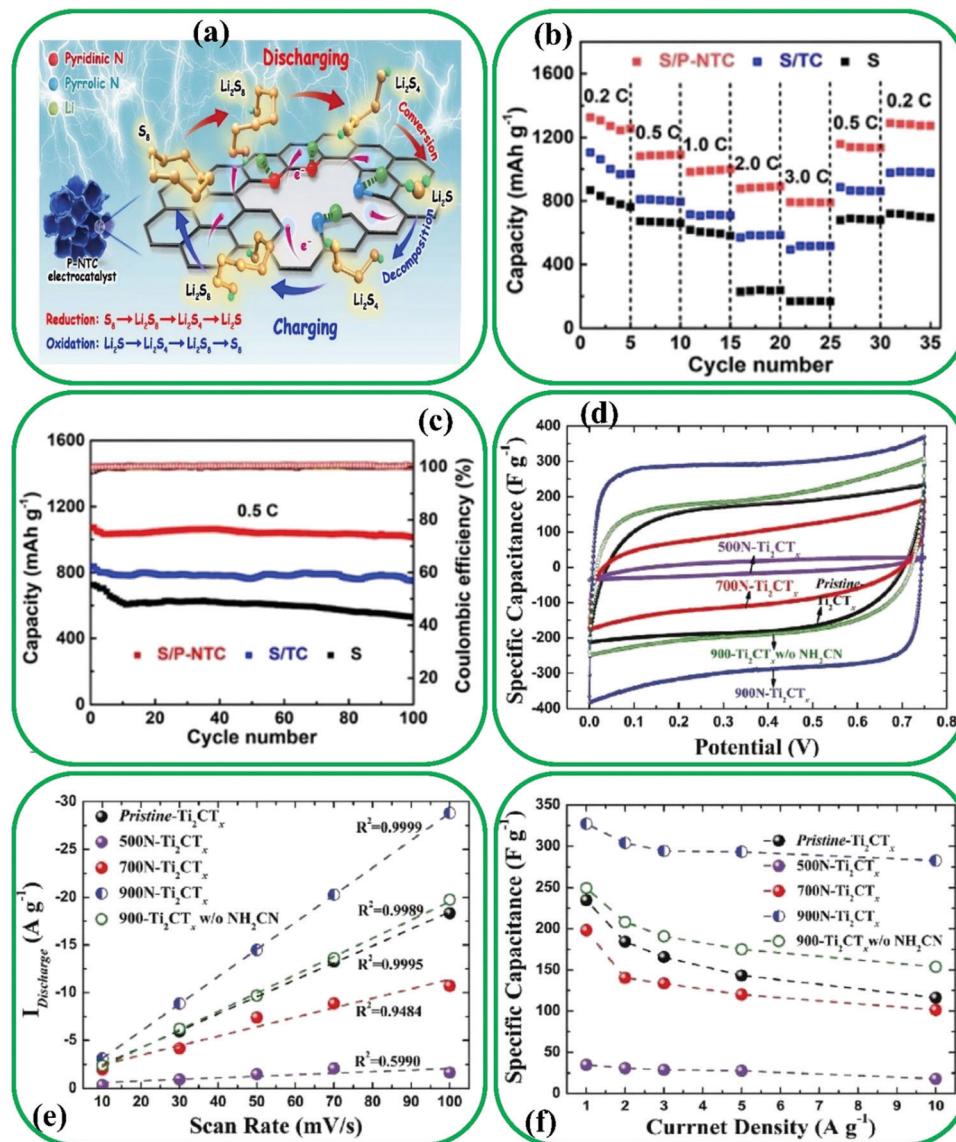
Fig. 18 (a) Schematic exhibition of the role of N-doped Ti₃C₂ in the Li–S cell. (b) Performance of the bare S cathode, pristine Ti₃C₂, and N-doped Ti₃C₂. (c) Cycling performance of S/N-doped Ti₃C₂ at 0.5 C. Reproduced with permission.[220] Copyright 2020, Elsevier. Electrochemical properties of pristine Ti₃C₂, 500N-Ti₃C₂, 700N-Ti₃C₂, 900N-Ti₃C₂, and 900N-Ti₃C₂ without NH₂CN electrodes with 6M KOH as the electrolyte; (d) comparison of cyclic voltammetry curves at a scan rate of 100 mV S⁻¹. (e) Discharge current densities as a function of scan rate. (f) Gravimetric specific capacitance at different current densities. Reproduced with permission.[118] Copyright 2018, Willey.

MXenes has been depicted in Fig. 18a, where numerous active sites are provided for the conversion and adsorption of LiPSs because MXenes have high electrical conductivity, large surface area, and porous structure. Besides, the interfacial interactions between the porous N-doped Ti_3C_2 MXenes and the Li_2S cluster were improved by the N doping process, which led to the degradation of the Li_2S dissociation barrier on the porous N-doped Ti_3C_2 MXenes and as well as the acceleration of the nucleation kinetics of Li_2S, thereby the decomposition reaction of Li_2S increases. Moreover, the sulfur redox kinetics are notably facilitated by the low diffusion barrier of Li atoms on the porous N-doped Ti_3C_2. The results showed that the prepared S-porous N-doped Ti_3C_2 cathode has higher capacities compared to the

S/Ti_3C_2 cathode and pristine S cathode (Fig. 18b). Fig. 18c shows the initial capacity and coulombic efficiency, where S-porous N-doped Ti_3C_2 MXenes exhibited superior performance at 0.5 C in comparison to those of S/Ti_3C_2 and pristine S cathode.[220]

4.4.1.1. Electrochemical capacitors. Electrochemical capacitors have attracted great interest because of their high power densities, long cycle life, and fast charge/discharge capabilities.[221] Among the various materials, MXene-based materials have received considerable attention owing to their superior electrical conductivity, excellent intercalation effects, and electrochemical energy storage characteristics.[159,222] It should be noted that the capacitive performance can be significantly affected by surface modification.[223]

For example, an N-doped Ti_2C MXene with various contents of N doping was prepared by carbon nitride decomposition and sequential intercalation *via* exfoliation and thermal annealing approach.[118] The capacitance performance of all pristine Ti_2C and N-doped Ti_2C demonstrated that as the annealing temperature increases, the cyclic voltammetry (CV) curve shape becomes more and more rectangular and the related surface areas increase (Fig. 18d). Indeed, the largest area observed for N-doped Ti_2C MXene at 900° suggests the high efficiency of the doping strategy. The discharge current densities of N-doped Ti_2C exhibit an approximately linear relationship with the scan rate, indicating that the fast electrochemical reaction occurred on the entire surface of the electrode (Fig. 18e). The highest specific capacitance of the N-doped Ti_2C electrode can attain 327 ± 1 F g^{-1} at 900 °C which is higher than those of the pristine Ti_2C and other N-doped-based MXene electrodes at different temperatures (Fig. 18f).

4.4.1.2. Metal-ion batteries. In the area of metal-ion batteries, including LIBs and SIBs, MXene-based materials have received considerable attention due to their kinetics and thermodynamics of metal-ion diffusion and intercalation in the lamellar space of MXenes. However, there are still unknowns such as the storage mechanism of metal ions, appropriate surface functional groups, and optimal MXene/metal ratios.[224,225]

The specific capacities of MXene-based materials are much lower than those of other electrode materials.[226] Hence, surface modification is a promising method to enhance the performance in SIBs and LIBs *via* combining the advantages of active sites and the conductivity of MXenes. For instance, the rate capability and the specific capacity of MXenes have been improved *via* surface modification through hydrothermal oxidation of TiO_2;[227–229] a specific capacity of 291 mA h g^{-1} for LIBs after 2000 cycles at a current density of 100 mA g^{-1}[230] was achieved. Liu *et al.* synthesized a novel N-doped Nb_2C MXene *via* a thermal reaction with urea.[81] Their N-doped Nb_2C MXene presented superior cycling stability and an excellent capacity of 360 mA h g^{-1} due to the improved specific surface area and electrical conductivity caused by the extension of the *c*-lattice parameter. Moreover, the surface chemistry of MXenes can be adjusted by cation modification.[29] The ion capacity of Sn^{4+} decorated V_2C MXenes was boosted to 1284 mA h g^{-1} at a density of 0.1 A g^{-1}, and the cycling stability reached a remarkable value of 1262.9 mA h g^{-1} after 90 cycles at the same density.[231] These improvements can be ascribed to the V–O–Sn bond and enlarged interlayer space, resulting in the fast charge transfer and interface ionic diffusion. Moreover, Guo *et al.* fabricated a 2D phosphorene/MXene hybrid anode with an *in situ* formed fluorinated interphase for LIB applications.[232] Their theoretical and experimental investigations showed that the combination of Ti_3C_2 and the 2D phosphorene heterostructure not only enhances the sodium diffusion but also alleviates the volume change of phosphorene. Furthermore, an in-depth X-ray photoelectron spectroscopy analysis demonstrated that the –F terminated MXene could enhance the Coulombic efficiencies and cyclic performances of the phosphorene/MXene hybrid anode by forming fluorine-rich compounds. As a result,

the phosphorene/$Ti_3C_2F_2$ presented excellent cycling performance (343 mA h g^{-1} after 1000 cycles at 1 A g^{-1}) and a superior reversible capacity of 535 mA h g^{-1} at 0.1 A g^{-1} compared to the fluorine-free electrolyte. Natu *et al.* reported that Ti_3AlC_2 can be etched and delaminated in various organic solvents in the presence of NH_4HF_2.[233] They found that the electrode capacity of the Ti_3C_2 etched in propylene carbonate (PC) was almost two times more than the same MXene synthesized in water when tested in NIB and that Ti_3C_2 rich in –F terminations can be synthesized using NH_4HF_2-containing polar organic solvents in the etching process.

Chen *et al.* investigated the experimental and theoretical influence of glycine functionalization of $Ti_3C_2O_2$ MXenes on charge storage because organic molecules can lead to enhanced interlayer space and hinder restacking.[54] The strong chemical reaction between glycine and $Ti_3C_2O_2$ MXenes was ascribed to the formation of the Ti–N bond *via* shared electrons between them. The interlayer spacing of pristine $Ti_3C_2O_2$ increased from 10.16 to 14.06 Å by surface functionalization (Fig. 19a and b), which leads to enhanced cycling performance, improved charging rate, and better ion accessibility. Surface functionalization of $Ti_3C_2O_2$ led to a high capacitance of 324 F g^{-1} at a scan rate of 10 mV s^{-1} (Fig. 19c), and also to an improved retention capacitance of 140 F g^{-1} for $Ti_3C_2O_2$/glycine electrodes, which is double the value for pristine $Ti_3C_2O_2$.

4.4.2. Energy conversion. The use of abundant solar energy allows the existing challenges in energy and environmental pollution to be addressed.[234] Solar energy can be directly converted to heat energy using 2D materials such as MXenes.[235] Photothermal energy conversion is extensively used in self-heating textiles,[236] seawater desalination,[237] and tumor treatment.[238] For instance, Yang *et al.* prepared PPy-modified Ti_3C_2 MXenes by *in situ* polymerization on the surface of Ti_3C_2 to enhance the antioxidant capacity and performance of photothermal energy conversion.[239] They then sprayed the PPy-modified MXenes (MXene@PPy) on a transparent film heater. Superior photothermal conversion of MXene@PPy can be obtained because of the synergistic effect of Ti_3C_2 and PPy. A comparison of the photothermal energy conversion performances of the pristine MXene and MXene@PPy films (Fig. 20a and b) indicated that under 200 mW cm^{-2} irradiation, the pristine MXene film showed tiny light-to-heat conversion along with a negligible increment in the temperature. In contrast, MXene@PPy was able to convert light to thermal energy more efficiently. The surface temperature increased from 25 to 61 °C. This enhancement in temperature confirmed the efficient photothermal conversion ability of MXene@PPy compared to the pristine MXene. After grafting PPy onto the MXene surface, the photothermal conversion performance is stable for approximately 7 months in air atmosphere. Du *et al.* synthesized a polymerized PDA-decorated MXene (Ti_3C_2@PDA) by *in situ* grafting of PDA on the surface of Ti_3C_2.[240] Fig. 20c illustrates the solar-thermal conversion performance of Ti_3C_2@PDA by calculation of the temperature evolution curves under 250 mW cm^{-2} irradiation. The solar-thermal efficiencies of a pristine film and an MXene-based film with 2%wt content of Ti_3C_2@PDA were reported to be 64.2% and 90.1%, respectively.
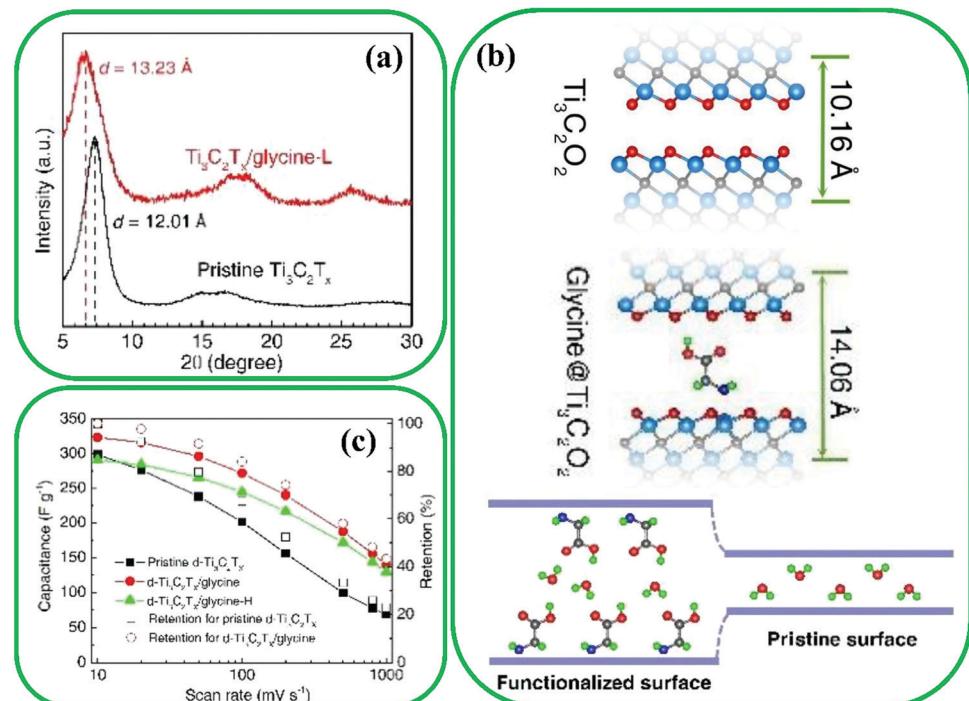
Fig. 19 (a) XRD patterns for pristine Ti_3C_2 and Ti_3C_2/glycine films. (b) Predicted interlayer spacing and schematic diagrams for pristine and glycine functionalized $Ti_3C_2O_2$. (c) Rate performance and capacitance retention for pristine and glycine functionalized $Ti_3C_2O_2$. Reproduced with permission.[54] Copyright 2018, The Royal Society of Chemistry.
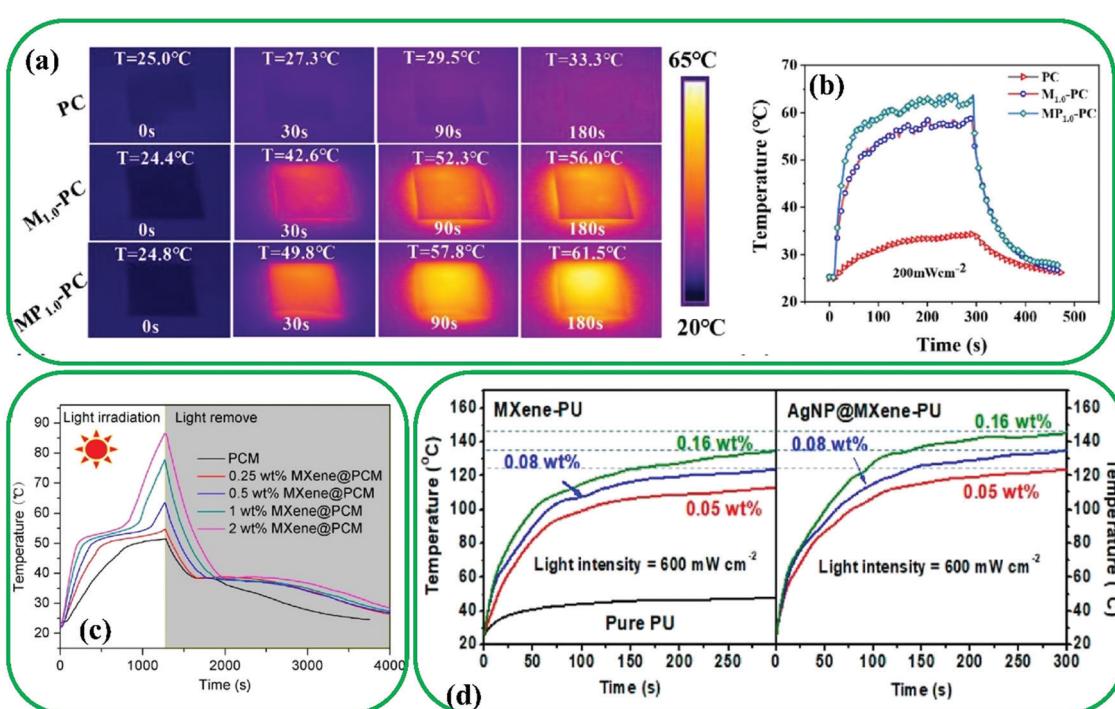

Fig. 20 (a) IR thermal images and (b) surface temperature evolution curves of different MXene@PPy-based films under 200 mW cm^{-2}. Reproduced with permission.[239] Copyright 2021, American Chemical Society. (c) Temperature evolution curves of pristine PCM and MXene@PCM at different concentrations of Ti_3C_2. Reproduced with permission.[240] Copyright 2020, American Chemical Society. (d) Temperature changes as a function of time for MXene-PU (left) and AgNP@MXene-PU (right) under 600 mW cm^{-2}. Reproduced with permission.[241] Copyright 2019, American Chemical Society.

It is obvious that the solar-thermal conversion performance of the organic phase change materials (PMCs) enhanced with the incorporation of Ti_3C_2@PDA. Furthermore, Fan et al. reported the introduction of silver nanoparticles (AgNPs) onto the surface of MXene for transparent device applications.[241] The obtained AgNP@MXene hybrid demonstrated a substantial temperature gain of 111 and 148 °C under the irradiation of 600 and 800 mW cm^{-2}, respectively. The effect of surface modification was evaluated by measuring the surface temperature of pristine MXene and AgNP@MXene hybrid at different time instants under vis-IR light (Fig. 20d). The significant discrepancy in the temperature of the AgNP@MXene hybrid shows the efficient conversion of light to thermal energy owing to the thermal conductivity and photothermal effect of MXenes with the plasmonic properties of AgNPs in conjunction.

4.5. Membrane-based separation

In the past few decades, many conventional techniques, including filtration, condensation, crystallization, and distillation, have been widely utilized in separation. However, membrane-based processes have emerged as a promising candidate for use in different applications such as water and wastewater treatment, and pharmaceutical and chemical industries.[242,243] Recently, MXene-based materials have been employed in membrane-based separation with high separation performance because of their large surface area, superior flexibility, and abundant surface functional groups.[13,244,245] This section reviews the effect of MXene-based materials on the separation performance of membranes and puts the advances into perspective.

4.5.1. Pervaporation. Membrane-based separation processes have attracted much attention in solvent dehydration because of their high energy efficiency and simplicity.[246,247] MXene-based materials have shown excellent separation performance, due to their good mechanical strength and excellent metallic conductivity.[248,249] It should be noted that enough care should be taken to achieve a defect-free layered structure for MXene-based membranes along with highly efficient solvent dehydration. Liu et al. prepared an ordered laminar structure of Ti_3C_2 MXene membrane by introducing positively charged polyelectrolytes (including PDDA, polyallylamine hydrochloride (PAH), and polyethylene (PEI)) to create electrostatic interactions with negatively charged Ti_3C_2 nanosheets (Fig. 21a) for pervaporation dehydration of isopropanol.[250] The lowest value of water contact angle for MXene–PDDA indicated that it can absorb more water molecules and facilitate the transport pathway of water, showing better separation performance compared to those of pristine MXene, MXene-PAH, and MXene–PEI membranes. As revealed in Fig. 21b, the MXene-PDDA membrane showed water content of ~99.5 wt%, while it was ~57, ~63, and ~18.9 wt% for the MXene–PAH, MXene–PEI, and pristine MXene membranes, respectively. The separation mechanism of the pervaporation process was described according to solution–diffusion;[251] the diffusion selectivity improved by the formation of regular packing of MXenes induced by PDDA introduction and the enhancement of water content may be related to the improvement of adsorption selectivity toward the water.

Moreover, water flux decreased when the PDDA concentrations increased from 0 to 0.36 mg mL^{-1}, suggesting an increase of transport resistance due to the occupation of transport pathways and enhanced membrane thickness.[252] However, the separation factor first increased and then decreased because of the promotion of selective diffusion and preferential sorption of water rather than isopropanol caused by the improvement of either the packing order of MXenes or hydrophilicity.

4.5.2. Nanofiltration. In another study, functionalized Ti_3C_2 MXenes were employed in thin-film nanocomposite membranes (TFNs) to improve selectivity and flux for alcohol-based solvents.[253] Four modifiers – APTES, (dodecyl)triethoxysilane (DCTES), (methyl aniline)triethoxysilane (MATES) and (γ-methacryloxypropyl)trimethoxysilane (MPTMS) – were employed to prepare functionalized $Ti_3C_2–NH_2$, $Ti_3C_2–C_{12}H_{26}$, $Ti_3C_2–C_6H_6$, and $Ti_3C_2–COOR$, respectively (Fig. 21c). The area swelling and solvent uptake of the prepared TFN membranes were evaluated with polar solvents (ethyl acetate and isopropanol) and non-polar solvents (n-heptane and toluene). As a result, the incorporation of Ti_3C_2 MXene led to the reduction of area swellings and solvent uptakes except for isopropanol due to its non-swelling characteristics. However, the storage and adsorption of isopropanol were promoted by the –OH groups on Ti_3C_2 through H-interaction. For the same reason, $Ti_3C_2–COOR$ and $Ti_3C_2–NH_2$ embedded TFN membranes demonstrated higher area swelling and solvent uptakes for polar solvents, while $Ti_3C_2–C_6H_6$ and $Ti_3C_2–C_{12}H_{26}$ exhibited higher area swelling and solvent uptakes toward non-polar solvents. All Ti_3C_2-M incorporated TFN membranes improved the affinity for a specific solvent based on the polarity properties of solvents and functional groups. This phenomenon can be ascribed to the fact that each of the four functional groups acts as a carrier and facilitates molecular transport through the TFN membranes. The affinity of $Ti_3C_2–NH_2$ and $Ti_3C_2–COOR$ incorporated membranes can be improved towards polar solvents. For example, –NH$_2$ can facilitate the transport of isopropanol molecules by acting as carrier sites. Similarly, embedding $Ti_3C_2–C_{12}H_{26}$ and $Ti_3C_2–C_6H_6$ enhances the transport of non-polar solvents. Adding a Ti_3C_2–M into the polymer matrix improves the rejection ability, and this could be related to the Ti_3C_2 and Ti_3C_2-M blocking the transport of molecules.

4.5.3. Desalination. MXene-based materials have provided a great opportunity to prepare membranes for seawater desalination.[255,256] MXene-based membranes have been synthesized to separate salts according to ionic charges and the hydration radius,[257] where the interlayer spacing can play a key role in salt separation. The surface modification of MXene nanosheets enhances the interlayer spacing, resulting in the improvement of selective separation.[258] Furthermore, it has been predicted that MXenes can show significant performance as a photothermal material along with the conversion of photo-to-thermal characteristics,[259] due to their rich surface chemistry and unique layered structure. For instance, Fei et al. prepared a novel solar steam generator with a highly efficient photothermal conversion of a cellulose acetate–MXene (CAM) membrane, which was synthesized by introducing the modified
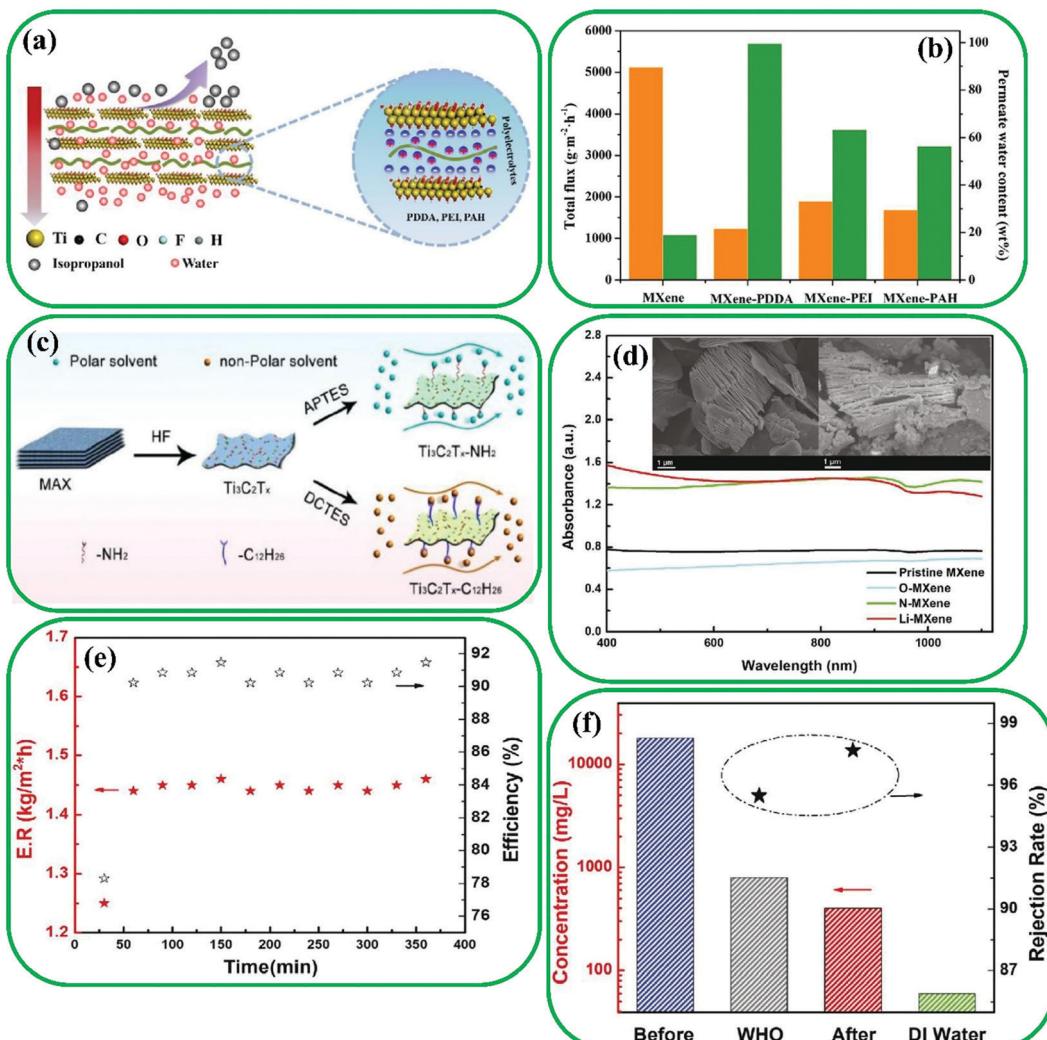
Fig. 21 (a) Schematic illustration of Ti₃C₂ laminar membranes functionalized via polyelectrolytes. (b) Effects of polyelectrolytes on MXene-based membranes for pervaporation dehydration of 90 wt% isopropanol/water at 50 °C. Reproduced with permission.[250] Copyright 2020, American Chemical Society. (c) Synthesis process of pristine Ti₃C₂ and functionalized Ti₃C₂ composites. Reproduced with permission.[253] Copyright 2017, Elsevier. (d) UV-vis absorbance spectrum of various powders. Inset: SEM images of MXene flakes, pristine MXene (left) and Li-MXene (right). (e) Energy conversion efficiency evaluation during continuous 6 h illumination. (f) Salt rejection rate revealed by ion concentration comparison before and after desalination showing the capability to produce drinking water. Reproduced with permission.[254] Copyright 2020, Wiley.

MXenes into the polymeric network of cellulose acetate.[254] Li-intercalated MXene (denoted as Li-MXene) possesses a high absorption rate (Fig. 21d) with high structural similarity to the pristine MXene. This may be attributed to the high photon absorption of Li-MXene in its structure and also to its black color, where lower lights are reflected. Measurement of the mass change demonstrated a remarkable enhancement of steam generation by the CAM membrane, which are ascribed to the superior photothermal characteristics of Li-MXene. Fig. 21e shows the energy conversion of the CAM membrane, where an efficiency of 92.1% was obtained after 11 cycles. In addition, a salt rejection of 97.7% was achieved for high salinity synthesized seawater (Na⁺ concentration of 18 000 mg L⁻¹) (Fig. 21f). These results showed that CAM membranes are good candidates for solar desalination applications because of their excellent robustness, scalability, and effectiveness.

4.5.4. Dye removal. Dyes are the major pollutants of discharged wastewater from industries, which can threaten human health issues because of their high carcinogenicity.[260] Therefore, the removal of dyes from wastewater should be considered as a major priority from an environmental viewpoint. Functionalized MXene-based membranes have exhibited promising potential for the removal of dyes from water and wastewater.[261,262] In this area, the interlayer spacing of MXenes plays a vital role in pressure-driven membrane processes because molecules larger than the interlayer spacing are rejected, and solvents are facilely penetrated.[22] Pandey et al. synthesized Ag@MXene membranes by grafting Ag on the surface of MXenes to enhance the interlayer spacing.[263] Accordingly, water flux increased by introducing Ag nanoparticles on the MXene surface compared to the pristine MXene-based membrane. This promotion can be due to the interlayer

voids of additional nanochannels by the presence of Ag nanoparticles, leading to facile water pathways. Besides, the Ag@M-Xene membranes exhibited high rejection of 100%, 92%, and 79.9% for bovine serum albumin (BSA), methyl green (MG), and rhodamine, respectively (Fig. 22a and b). Flux recovery of membranes needs to be evaluated to understand the membrane fouling properties. The Ag@MXene membranes after exposure to BSA and MG indicated 91% and 97% of flux recovery compared to 81% and 86% for the pristine MXene membrane.

4.5.5. Gas separation. Another field that MXene-based materials have impacted is the area of membrane-based gas separation, which is growing due to the low energy consumption and high efficiency of these processes.[265] Different kinds of 2D materials, such as metal–organic frameworks (MOFs),[266,267] covalent-organic frameworks (COFs),[268] zeolites,[269] and

graphene,[270] have been extensively employed for improving the gas separation performance of membranes by surpassing the trade-off relationship between permeability and selectivity.[271] MXene-based materials are attractive to further improve the gas separation performance by tuning the interlayer spacing, as gas molecules larger than the interlayer spacing are prevented from passing through.[272] The extraordinary separation performance of MXene-based membranes, such as favorable mechanical stability and good reproducibility due to the existence of ordered channels in lamellar MXene membranes, has been reported.[272] The surface modification of MXene nanosheets can improve the interlayer space, resulting in enhanced selective molecular separation. Shen *et al.* prepared a MXene-based nanofilm on an anodic aluminum oxide (AAO) substrate for H_2/CO_2 separation (Fig. 22c).[264] The pristine MXene nanofilm with 20 nm thickness showed high permeance of 1584 GPU and H_2/CO_2 selectivity of 27, which
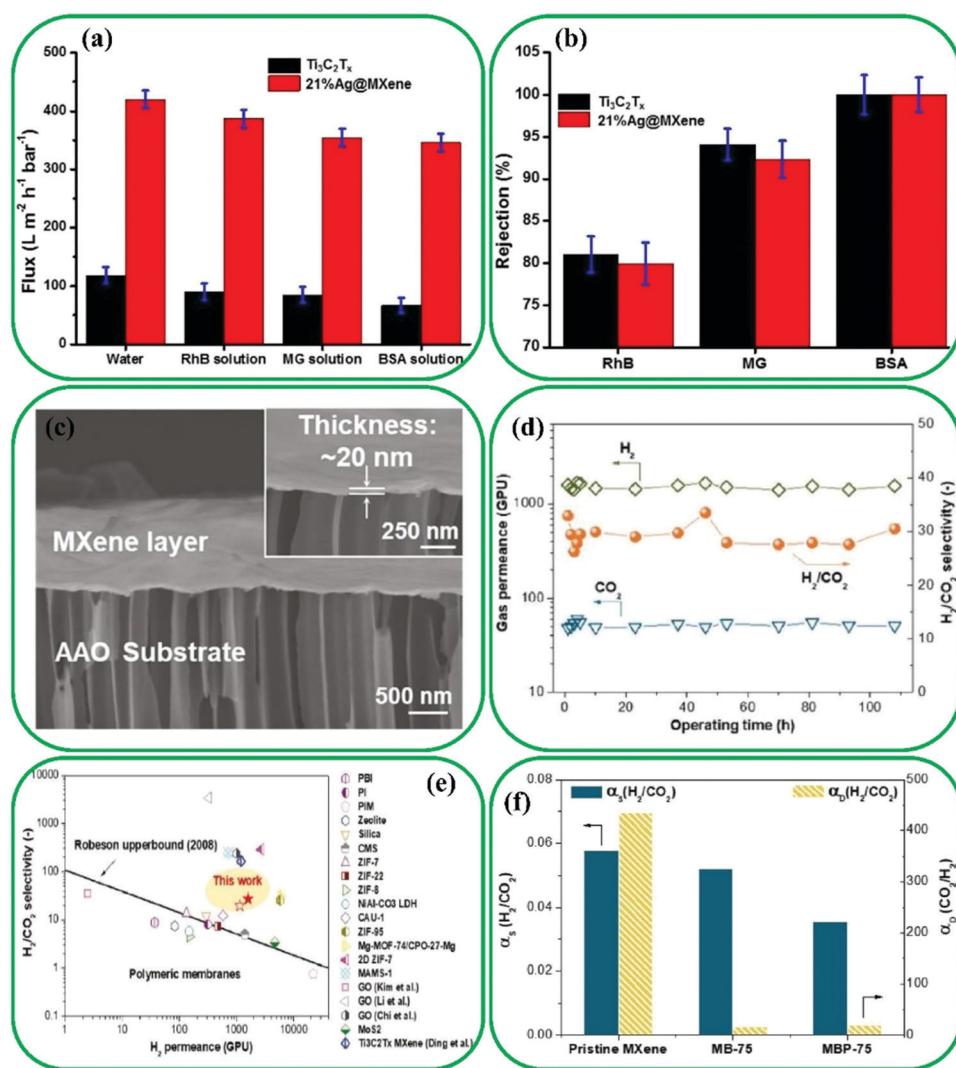
Fig. 22 Comparison of the performance of the pristine Ti_3C_2 and 21%Ag@Ti_3C_2 membranes for the separation of RhB, MG, and BSA molecules at 25 °C: (a) flux and (b) rejection. Reproduced with permission.[263] Copyright 2018, The Royal Society of Chemistry. (c) Cross-section SEM image of MXene nanofilms. (d) Long-term gas transport properties of H_2-selective MXene nanofilms. (e) H_2/CO_2 separation compared with state-of-the-art gas separation membranes. (f) Sorption selectivity (α_s) as well as diffusion selectivity (α_D) of H_2/CO_2 for various MXene-based nanofilms. Reproduced with permission.[264] Copyright 2018, Wiley.

exceeded the Robeson upper-bound. Besides, it is worth noting that this kind of membrane exhibited stable performance during 100 h of continuous long-term operation (Fig. 22d). Borate and polyethylenimine (PEI) were introduced between the MXene nanosheets to assess the gas transport behavior of CO_2 capture. Borate can not only facilitate the transport of CO_2 molecules with reversible reactions for the enhancement of CO_2 permeance, but can also crosslink with the –O groups on MXenes to decrease the interlayer spacing for promoting the selectivity of CO_2/N_2 and CO_2/CH_4. Furthermore, strong electrostatic interactions can be formed between the positively charged PEI and negatively charged MXene with the possible reaction of Ti suboxides and amine groups on PEI. Excellent gas separation was obtained for functionalized MXene nanofilms (Fig. 22e). The investigation of gas separation mechanism of pristine and functionalized MXene nanofilms demonstrated that pristine MXene membranes are diffusion-controlled, while borate and PEI functionalized MXene nanofilms indicated CO_2 selective separation (Fig. 22f) because of the CO_2-philic nature of borate and PEI.

Currently, there is a need for studies to understand how factors such as gas mixture composition, the size of MXene nanosheets, the interaction between MXene nanosheets and gas molecules, and various surface terminations affect gas selectivity and permeability.

5. Conclusion and perspective

In the past decade, MXenes have received considerable attention because of their appealing properties such as physicochemical, mechanical, magnetic and electronic characteristics, abundant surface terminations, and great surface area. As such, they have found applications in many areas such as biomedicine, sensing, catalysis, energy storage and conversion, and membrane-based separation. Surface functionalization of MXenes allows the alteration of various properties of MXenes, further increasing their versatility and enabling their weaknesses such as poor stability in the presence of water and molecular oxygen, facile restacking, and low flexibility to be addressed. This article reviewed the recent advances in MXene surface functionalization methods, MXene-affected properties, and the practical applications of the resulting surface-modified MXenes. Surface-modified MXenes have demonstrated great potential for use in different applications. Previous studies indicate that for every specific application, a modified MXene that outperforms the pristine MXene can be fabricated. In spite of many reported studies on surface functionalization of MXenes, there are still challenges and opportunities in this area. Examples are as follows:

1. An MXene with desired concentrations of termination groups and interlayer spacing is essential to prepare surface-modified MXene materials for different applications.

2. In catalysis, the exact mechanisms *via* which pristine and surface-modified MXenes promote reactions and the role of active sites on their surface are not well understood. Hence, computational and experimental studies are needed to improve the understanding, allowing the invention of novel catalysts.

3. In biomedical applications, MXene-based materials have shown great potential and low toxicity. However, the effect of toxicity of pristine and surface-modified MXenes on humans and the environment has not been investigated yet.

4. The water dispersity of MXenes can be improved *via* surface modification with hydrophilic polymers. However, these surface-modified MXenes are not stable adequately under some excessive conditions. Thus, better functionalization approaches are needed to form covalent and dynamic bonds. Besides, the effect of surface functionalization on biocompatibility needs to be explored further.

5. For application in sensors and photodetectors, performances of pristine and surface functionalized MXenes such as sensitivity and responsivity are still limited. Furthermore, the weight and size of pristine and surface functionalized MXene-based sensors need to be reduced for practical applications, especially for biomedical sensors. Therefore, energy-efficient, highly sensitive, super-small, and intelligent sensors and photodetectors should be developed.

6. It has been demonstrated that the interlayer spacing and surface functional groups of pristine and surface-modified MXenes have a great influence on their performance and structure. However, the impact of every single functional group on the performance of supercapacitors and batteries has not been studied; the relationship between the physicochemical characteristics and every single termination group is very important to understand.

7. For LIBs, the first cycle coulombic efficiency should be adequately enhanced by either modifying the anode/electrode interface or developing the surface chemistry of MXenes. The interface functionalization can be performed by providing an artificial layer of solid electrolyte interface on the MXene electrode, which leads to hindering undesirable reactions and does not prevent the Li^+ ion diffusion.

8. Pristine and surface-modified MXenes are promising candidates for separation applications due to their outstanding features. However, easy tuning of the interlayer spacing and reducing the degradation of MXenes materials should be addressed.

9. It is essential to master tailoring of the surface chemistry of MXenes by post-etch processing, which facilitates the surface modification of MXenes and enhances MXene properties. The effect of individual functional group in each application needs to be investigated further *via ex situ* and *in situ* characterization studies.

Conflicts of interest

There are no conflicts to declare.

Acknowledgements

References

1 S. Stankovich, D. A. Dikin, G. H. Dommett, K. M. Kohlhaas, E. J. Zimney, E. A. Stach, R. D. Piner, S. T. Nguyen and R. S. Ruoff, *Nature*, 2006, **442**, 282–286.

2 E. Benavente, M. Santa Ana, F. Mendizábal and G. González, *Coord. Chem. Rev.*, 2002, **224**, 87–109.

3 W. Chen, J. Ouyang, H. Liu, M. Chen, K. Zeng, J. Sheng, Z. Liu, Y. Han, L. Wang and J. Li, *Adv. Mater.*, 2017, **29**, 1603864.

4 C. R. Martin, *Science*, 1994, **266**, 1961–1966.

5 A. Shahzad, K. Rasool, M. Nawaz, W. Miran, J. Jang, M. Moztahida, K. A. Mahmoud and D. S. Lee, *Chem. Eng. J.*, 2018, **349**, 748–755.

6 Y. Wu, P. Nie, L. Wu, H. Dou and X. Zhang, *Chem. Eng. J.*, 2018, **334**, 932–938.

7 S. Sun, C. Liao, A. M. Hafez, H. Zhu and S. Wu, *Chem. Eng. J.*, 2018, **338**, 27–45.

8 C. Ding, J. Liang, Z. Zhou, Y. Li, W. Peng, G. Zhang, F. Zhang and X. Fan, *Chem. Eng. J.*, 2019, **378**, 122205.

9 Z. Xiao, S. Ruan, L. B. Kong, W. Que, K. Zhou, Y. Liu and T. Zhang, *Springer Nature*, 2020.

10 M. Naguib, V. N. Mochalin, M. W. Barsoum and Y. Gogotsi, *Adv. Mater.*, 2014, **26**, 992–1005.

11 M. Naguib, M. Kurtoglu, V. Presser, J. Lu, J. Niu, M. Heon, L. Hultman, Y. Gogotsi and M. W. Barsoum, *Adv. Mater.*, 2011, **23**, 4248–4253.

12 M. W. Barsoum, *MAX phases: properties of machinable ternary carbides and nitrides*, John Wiley & Sons, 2013.

13 H. Riazi, M. Anayee, K. Hantanasirisakul, A. A. Shamsabadi, B. Anasori, Y. Gogotsi and M. Soroush, *Adv. Mater. Interfaces*, 2020, **7**, 1902008.

14 X. Wu, X. Cui, W. Wu, J. Wang, Y. Li and Z. Jiang, *Angew. Chem., Int. Ed.*, 2019, **58**, 18524–18529.

15 L. Verger, V. Natu, M. Carey and M. W. Barsoum, *Trends Chem.*, 2019, **1**, 656–669.

16 J. Chen, Q. Huang, H. Huang, L. Mao, M. Liu, X. Zhang and Y. Wei, *Nanoscale*, 2020, **12**, 3574–3592.

17 M. Magnuson, J. Halim and L.-Å. Näslund, *J. Electron Spectrosc. Relat. Phenom.*, 2018, **224**, 27–32.

18 H. Lin, L. Chen, X. Lu, H. Yao, Y. Chen and J. Shi, *Sci. China: Mater.*, 2019, **62**, 662–670.

19 S. Zhang, H. Zhuo, S. Li, Z. Bao, S. Deng, G. Zhuang, X. Zhong, Z. Wei, Z. Yao and J.-G. Wang, *Catal. Today*, 2021, **368**, 187–195.

20 A. Shahzad, M. Nawaz, M. Moztahida, J. Jang, K. Tahir, J. Kim, Y. Lim, V. S. Vassiliadis, S. H. Woo and D. S. Lee, *Chem. Eng. J.*, 2019, **368**, 400–408.

21 C. Peng, P. Wei, X. Chen, Y. Zhang, F. Zhu, Y. Cao, H. Wang, H. Yu and F. Peng, *Ceram. Int.*, 2018, **44**, 18886–18893.

22 J. Li, X. Li and B. Van der Bruggen, *Environ. Sci.: Nano*, 2020, **7**, 1289–1304.

23 H. E. Karahan, K. Goh, C. Zhang, E. Yang, C. Yıldırım, C. Y. Chuah, M. G. Ahunbay, J. Lee, Ş. B. Tantekin-Ersolmaz and Y. Chen, *Adv. Mater.*, 2020, **32**, 1906697.

24 Y. A. J. Al-Hamadani, B.-M. Jun, M. Yoon, N. Taheri-Qazvini, S. A. Snyder, M. Jang, J. Heo and Y. Yoon, *Chemosphere*, 2020, **254**, 126821.

25 L. Gao, C. Li, W. Huang, S. Mei, H. Lin, Q. Ou, Y. Zhang, J. Guo, F. Zhang and S. Xu, *Chem. Mater.*, 2020, **32**, 1703–1747.

26 W. Huang, L. Hu, Y. Tang, Z. Xie and H. Zhang, *Adv. Funct. Mater.*, 2020, **30**, 2005223.

27 S. Cao, B. Shen, T. Tong, J. Fu and J. Yu, *Adv. Funct. Mater.*, 2018, **28**, 1800136.

28 X. Zhang, Z. Zhang and Z. Zhou, *J. Energy Chem.*, 2018, **27**, 73–85.

29 X. Hui, X. Ge, R. Zhao, Z. Li and L. Yin, *Adv. Funct. Mater.*, 2020, **30**, 2005190.

30 E. Pomerantseva and Y. Gogotsi, *Nat. Energy*, 2017, **2**, 1–6.

31 S. J. Kim, H.-J. Koh, C. E. Ren, O. Kwon, K. Maleski, S.-Y. Cho, B. Anasori, C.-K. Kim, Y.-K. Choi and J. Kim, *ACS Nano*, 2018, **12**, 986–993.

32 H. L. Chia, C. C. Mayorga-Martinez, N. Antonatos, Z. K. Sofer, J. J. Gonzalez-Julian, R. D. Webster and M. Pumera, *Anal. Chem.*, 2020, **92**, 2452–2459.

33 F. Shahzad, A. Iqbal, S. A. Zaidi, S.-W. Hwang and C. M. Koo, *J. Ind. Eng. Chem.*, 2019, **79**, 338–344.

34 S. M. George and B. Kandasubramanian, *Ceram. Int.*, 2020, **46**, 8522–8535.

35 H. Lin, X. Wang, L. Yu, Y. Chen and J. Shi, *Nano Lett.*, 2017, **17**, 384–391.

36 K. Huang, Z. Li, J. Lin, G. Han and P. Huang, *Chem. Soc. Rev.*, 2018, **47**, 5109–5124.

37 X. Han, J. Huang, H. Lin, Z. Wang, P. Li and Y. Chen, *Adv. Healthcare Mater.*, 2018, **7**, 1701394.

38 H. Ouyang, M. Zhou, Y. Guo, M. He, H. Huang, X. Ye, Y. Feng, X. Zhou and S. Yang, *Fitoterapia*, 2014, **96**, 152–158.

39 X. Zhang, J. Li, B. Xie, B. Wu, S. Lei, Y. Yao, M. He, H. Ouyang, Y. Feng and W. Xu, *Front. Pharmacol.*, 2018, **9**, 282.

40 X. Zhang, M. He, S. Lei, B. Wu, T. Tan, H. Ouyang, W. Xu and Y. Feng, *J. Pharm. Biomed. Anal.*, 2018, **156**, 221–231.

41 Y. Xie, M. Naguib, V. N. Mochalin, M. W. Barsoum, Y. Gogotsi, X. Yu, K.-W. Nam, X.-Q. Yang, A. I. Kolesnikov and P. R. Kent, *J. Am. Chem. Soc.*, 2014, **136**, 6385–6394.

42 K. Chen, N. Qiu, Q. Deng, M.-H. Kang, H. Yang, J.-U. Baek, Y.-H. Koh, S. Du, Q. Huang and H.-E. Kim, *ACS Biomater. Sci. Eng.*, 2017, **3**, 2293–2301.

43 M. Mozafari, A. Arabi Shamsabadi, A. Rahimpour and M. Soroush, *Adv. Mater. Technol.*, 2021, 2001189.

44 M. Alhabeb, K. Maleski, B. Anasori, P. Lelyukh, L. Clark, S. Sin and Y. Gogotsi, *Chem. Mater.*, 2017, **29**, 7633–7644.

45 J. Jeon, Y. Park, S. Choi, J. Lee, S. S. Lim, B. H. Lee, Y. J. Song, J. H. Cho, Y. H. Jang and S. Lee, *ACS Nano*, 2018, **12**, 338–346.

46 O. Mashtalir, K. M. Cook, V. N. Mochalin, M. Crowe, M. W. Barsoum and Y. Gogotsi, *J. Mater. Chem. A*, 2014, **2**, 14334–14338.

47 X.-H. Zha, Q. Huang, J. He, H. He, J. Zhai, J. S. Francisco and S. Du, *Sci. Rep.*, 2016, **6**, 1–10.

48 C. J. Zhang, S. Pinilla, N. McEvoy, C. P. Cullen, B. Anasori, E. Long, S.-H. Park, A. S. Seral-Ascaso, A. Shmeliov and D. Krishnan, *Chem. Mater.*, 2017, **29**, 4848–4856.

49 A. Rozmysłowska, T. Wojciechowski, W. Ziemkowska, L. Chlubny, A. Olszyna, S. Poźniak, K. Tomkiewicz and A. Jastrzębska, *Int. J. Electrochem. Sci.*, 2018, **13**, 10837–10847.

50 H. Lin, Y. Wang, S. Gao, Y. Chen and J. Shi, *Adv. Mater.*, 2018, **30**, 1703284.

51 Z. Friedman, K. H. Marks, M. J. Maisels, R. Thorson and R. Naeye, *Pediatrics*, 1978, **61**, 694–698.

52 S. Wang, Y. Liu, Q.-F. Lü and H. Zhuang, *J. Mol. Liq.*, 2020, **297**, 111810.

53 A. C. Rajan, A. Mishra, S. Satsangi, R. Vaish, H. Mizuseki, K.-R. Lee and A. K. Singh, *Chem. Mater.*, 2018, **30**, 4031–4038.

54 Z. Li, Z. Zhuang, F. Lv, H. Zhu, L. Zhou, M. Luo, J. Zhu, Z. Lang, S. Feng and W. Chen, *Adv. Mater.*, 2018, **30**, 1803220.

55 Y. Xia, T. S. Mathis, M.-Q. Zhao, B. Anasori, A. Dang, Z. Zhou, H. Cho, Y. Gogotsi and S. Yang, *Nature*, 2018, **557**, 409–412.

56 Z. Huang, S. Wang, S. Kota, Q. Pan, M. W. Barsoum and C. Y. Li, *Polymer*, 2016, **102**, 119–126.

57 W. Shao, M. Tebyetekerwa, I. Marriam, W. Li, Y. Wu, S. Peng, S. Ramakrishna, S. Yang and M. Zhu, *J. Power Sources*, 2018, **396**, 683–690.

58 J. Chen, M. Liu, H. Huang, F. Deng, L. Mao, Y. Wen, L. Huang, J. Tian, X. Zhang and Y. Wei, *J. Mol. Liq.*, 2018, **259**, 179–185.

59 X. Zhang, K. Wang, M. Liu, X. Zhang, L. Tao, Y. Chen and Y. Wei, *Nanoscale*, 2015, **7**, 11486–11508.

60 M. Liu, G. Zeng, K. Wang, Q. Wan, L. Tao, X. Zhang and Y. Wei, *Nanoscale*, 2016, **8**, 16819–16840.

61 H. Wang, J. Zhang, Y. Wu, H. Huang, G. Li, X. Zhang and Z. Wang, *Appl. Surf. Sci.*, 2016, **384**, 287–293.

62 X. Zhu, B. Liu, H. Hou, Z. Huang, K. M. Zeinu, L. Huang, X. Yuan, D. Guo, J. Hu and J. Yang, *Electrochim. Acta*, 2017, **248**, 46–57.

63 Y. Tian, W. Que, Y. Luo, C. Yang, X. Yin and L. B. Kong, *J. Mater. Chem. A*, 2019, 7, 5416–5425.

64 P. Liu, W. Ding, J. Liu, L. Shen, F. Jiang, P. Liu, Z. Zhu, G. Zhang, C. Liu and J. Xu, *J. Alloys Compd.*, 2020, **829**, 154634.

65 M. Boota, B. Anasori, C. Voigt, M. Q. Zhao, M. W. Barsoum and Y. Gogotsi, *Adv. Mater.*, 2016, **28**, 1517–1522.

66 L. Qin, Q. Tao, X. Liu, M. Fahlman, J. Halim, P. O. Persson, J. Rosen and F. Zhang, *Nano Energy*, 2019, **60**, 734–742.

67 R. Jiang, M. Liu, H. Huang, L. Mao, Q. Huang, Y. Wen, Q.-Y. Cao, J. Tian, X. Zhang and Y. Wei, *Dyes Pigm.*, 2018, **153**, 99–105.

68 Z. Long, M. Liu, R. Jiang, Q. Wan, L. Mao, Y. Wan, F. Deng, X. Zhang and Y. Wei, *Chem. Eng. J.*, 2017, **308**, 527–534.

69 Q. Wan, Q. Huang, M. Liu, D. Xu, H. Huang, X. Zhang and Y. Wei, *Appl. Mater. Today*, 2017, **9**, 145–160.

70 R. Jiang, M. Liu, C. Li, Q. Huang, H. Huang, Q. Wan, Y. Wen, Q.-Y. Cao, X. Zhang and Y. Wei, *Mater. Sci. Eng., C*, 2017, **80**, 708–714.

71 L. Huang, S. Yang, J. Chen, J. Tian, Q. Huang, H. Huang, Y. Wen, F. Deng, X. Zhang and Y. Wei, *Mater. Sci. Eng., C*, 2019, **94**, 270–278.

72 R. Jiang, X. Xiao, J. Zheng, M. Chen and L. Chen, *Mater. Chem. Phys.*, 2020, **242**, 122529.

73 Z. Jin, Y. Fang, X. Wang, G. Xu, S. Wei, C. Zhou, Y. Zhang and Y. Xu, *J. Colloid Interface Sci.*, 2019, **537**, 306–315.

74 F. Shahzad, M. Alhabeb, C. B. Hatter, B. Anasori, S. M. Hong, C. M. Koo and Y. Gogotsi, *Science*, 2016, **353**, 1137–1140.

75 R. Sun, H. B. Zhang, J. Liu, X. Xie, R. Yang, Y. Li, S. Hong and Z. Z. Yu, *Adv. Funct. Mater.*, 2017, **27**, 1702807.

76 Z. Ling, C. E. Ren, M.-Q. Zhao, J. Yang, J. M. Giammarco, J. Qiu, M. W. Barsoum and Y. Gogotsi, *Proc. Natl. Acad. Sci. U. S. A.*, 2014, **111**, 16676–16681.

77 Z. W. Gao, W. Zheng and L. Y. S. Lee, *Small*, 2019, **15**, 1902649.

78 X. Liang, A. Garsuch and L. F. Nazar, *Angew. Chem.*, 2015, **127**, 3979–3983.

79 W. Bao, C. E. Shuck, W. Zhang, X. Guo, Y. Gogotsi and G. Wang, *ACS Nano*, 2019, **13**, 11500–11509.

80 H. Li, X. Wang, H. Li, S. Lin, B. Zhao, J. Dai, W. Song, X. Zhu and Y. Sun, *J. Alloys Compd.*, 2019, **784**, 923–930.

81 R. Liu, W. Cao, D. Han, Y. Mo, H. Zeng, H. Yang and W. Li, *J. Alloys Compd.*, 2019, **793**, 505–511.

82 Y. Yoon, A. P. Tiwari, M. Choi, T. G. Novak, W. Song, H. Chang, T. Zyung, S. S. Lee, S. Jeon and K. S. An, *Adv. Funct. Mater.*, 2019, **29**, 1903443.

83 C. Wang, S. Chen and L. Song, *Adv. Funct. Mater.*, 2020, **30**, 2000869.

84 R. Thakur, A. VahidMohammadi, J. Moncada, W. R. Adams, M. Chi, B. Tatarchuk, M. Beidaghi and C. A. Carrero, *Nanoscale*, 2019, **11**, 10716–10726.

85 O. Mashtalir, M. Naguib, B. Dyatkin, Y. Gogotsi and M. W. Barsoum, *Mater. Chem. Phys.*, 2013, **139**, 147–152.

86 T. Schultz, N. C. Frey, K. Hantanasirisakul, S. Park, S. J. May, V. B. Shenoy, Y. Gogotsi and N. Koch, *Chem. Mater.*, 2019, **31**, 6590–6597.

87 J. L. Hart, K. Hantanasirisakul, A. C. Lang, B. Anasori, D. Pinto, Y. Pivak, J. T. van Omme, S. J. May, Y. Gogotsi and M. L. Taheri, *Nat. Commun.*, 2019, **10**, 1–10.

88 D. Zhang, S. Wang, R. Hu, J. Gu, Y. Cui, B. Li, W. Chen, C. Liu, J. Shang and S. Yang, *Adv. Funct. Mater.*, 2020, **30**, 2002471.

89 Y. Lei, Y. Cui, Q. Huang, J. Dou, D. Gan, F. Deng, M. Liu, X. Li, X. Zhang and Y. Wei, *Ceram. Int.*, 2019, **45**, 17653–17661.

90 S. Kumar, Y. Lei, N. H. Alshareef, M. Quevedo-Lopez and K. N. Salama, *Biosens. Bioelectron.*, 2018, **121**, 243–249.

91 H. Wang, J. Zhang, Y. Wu, H. Huang and Q. Jiang, *J. Phys. Chem. Solids*, 2018, **115**, 172–179.

92 M. A. Iqbal, S. I. Ali, F. Amin, A. Tariq, M. Z. Iqbal and S. Rizwan, *ACS Omega*, 2019, **4**, 8661–8668.

93 A. Tariq, S. I. Ali, D. Akinwande and S. Rizwan, *ACS Omega*, 2018, **3**, 13828–13836.

94 R. Wu, H. Du, Z. Wang, M. Gao, H. Pan and Y. Liu, *J. Power Sources*, 2016, **327**, 519–525.

95 X. Wu, L. Hao, J. Zhang, X. Zhang, J. Wang and J. Liu, *J. Membr. Sci.*, 2016, **515**, 175–188.

96 Y. Jiang, X. Xie, Y. Chen, Y. Liu, R. Yang and G. Sui, *J. Mater. Chem. C*, 2018, **6**, 8679–8687.

97 W.-T. Cao, F.-F. Chen, Y.-J. Zhu, Y.-G. Zhang, Y.-Y. Jiang, M.-G. Ma and F. Chen, *ACS Nano*, 2018, **12**, 4583–4593.

98 J. Chen, K. Chen, D. Tong, Y. Huang, J. Zhang, J. Xue, Q. Huang and T. Chen, *Chem. Commun.*, 2015, **51**, 314–317.

99 C. Chen, M. Boota, X. Xie, M. Zhao, B. Anasori, C. E. Ren, L. Miao, J. Jiang and Y. Gogotsi, *J. Mater. Chem. A*, 2017, **5**, 5260–5265.

100 Z. Zhang, S. Yang, P. Zhang, J. Zhang, G. Chen and X. Feng, *Nat. Commun.*, 2019, **10**, 1–9.

101 G. S. Gund, J. H. Park, R. Harpalsinh, M. Kota, J. H. Shin, T.-I. Kim, Y. Gogotsi and H. S. Park, *Joule*, 2019, **3**, 164–176.

102 S. Tu, Q. Jiang, X. Zhang and H. N. Alshareef, *ACS Nano*, 2018, **12**, 3369–3377.

103 M. Carey, Z. Hinton, M. Sokol, N. J. Alvarez and M. W. Barsoum, *ACS Appl. Mater. Interfaces*, 2019, **11**, 20425–20436.

104 Q. W. Wang, H. B. Zhang, J. Liu, S. Zhao, X. Xie, L. Liu, R. Yang, N. Koratkar and Z. Z. Yu, *Adv. Funct. Mater.*, 2019, **29**, 1806819.

105 J. Xuan, Z. Wang, Y. Chen, D. Liang, L. Cheng, X. Yang, Z. Liu, R. Ma, T. Sasaki and F. Geng, *Angew. Chem.*, 2016, **128**, 14789–14794.

106 N. Tao, D. Zhang, X. Li, D. Lou, X. Sun, C. Wei, J. Li, J. Yang and Y.-N. Liu, *Chem. Sci.*, 2019, **10**, 10765–10771.

107 X. Li, J. Zhu, L. Wang, W. Wu and Y. Fang, *Electrochim. Acta*, 2017, **258**, 291–301.

108 H. Wang, L. Li, C. Zhu, S. Lin, J. Wen, Q. Jin and X. Zhang, *J. Alloys Compd.*, 2019, **778**, 858–865.

109 A. A. Shamsabadi, F. Seidi, E. Salehi, M. Nozari, A. Rahimpour and M. Soroush, *J. Mater. Chem. A*, 2017, **5**, 4011–4025.

110 Z. Nie, A. Petukhova and E. Kumacheva, *Nat. Nanotechnol.*, 2010, **5**, 15–25.

111 L. Fu, Z. Yan, Q. Zhao and H. Yang, *Adv. Mater. Interfaces*, 2018, **5**, 1801094.

112 S. B. Ambade, R. B. Ambade, W. Eom, S. H. Noh, S. H. Kim and T. H. Han, *Adv. Mater. Interfaces*, 2018, **5**, 1801361.

113 A. Ali, K. Hantanasirisakul, A. Abdala, P. Urbankowski, M.-Q. Zhao, B. Anasori, Y. Gogotsi, B. Aïssa and K. A. Mahmoud, *Langmuir*, 2018, **34**, 11325–11334.

114 A. VahidMohammadi, J. Moncada, H. Chen, E. Kayali, J. Orangi, C. A. Carrero and M. Beidaghi, *J. Mater. Chem. A*, 2018, **6**, 22123–22133.

115 J. Li, D. Yan, S. Hou, Y. Li, T. Lu, Y. Yao and L. Pan, *J. Mater. Chem. A*, 2018, **6**, 1234–1243.

116 C. Lu, L. Yang, B. Yan, L. Sun, P. Zhang, W. Zhang and Z. Sun, *Adv. Funct. Mater.*, 2020, **30**, 2000852.

117 L. Yu, Z. Fan, Y. Shao, Z. Tian, J. Sun and Z. Liu, *Adv. Energy Mater.*, 2019, **9**, 1901839.

118 Y. Yoon, M. Lee, S. K. Kim, G. Bae, W. Song, S. Myung, J. Lim, S. S. Lee, T. Zyung and K. S. An, *Adv. Energy Mater.*, 2018, **8**, 1703173.

119 E. Balcı, Ü. Ö. Akkuş and S. Berber, *J. Condens. Matter Phys.*, 2018, **30**, 155501.

120 S. Zheng, S. Li, Z. Mei, Z. Hu, M. Chu, J. Liu, X. Chen and F. Pan, *J. Phys. Chem. Lett.*, 2019, **10**, 6984–6989.

121 D. Kan, D. Wang, X. Zhang, R. Lian, J. Xu, G. Chen and Y. Wei, *J. Mater. Chem. A*, 2020, **8**, 3097–3108.

122 Y. Liu, H. Xiao and W. A. Goddard III, *J. Am. Chem. Soc.*, 2016, **138**, 15853–15856.

123 M. Khazaei, M. Arai, T. Sasaki, A. Ranjbar, Y. Liang and S. Yunoki, *Phys. Rev. B: Condens. Matter Mater. Phys.*, 2015, **92**, 075411.

124 M. Naguib, J. Halim, J. Lu, K. M. Cook, L. Hultman, Y. Gogotsi and M. W. Barsoum, *J. Am. Chem. Soc.*, 2013, **135**, 15966–15969.

125 J. Halim, S. Kota, M. R. Lukatskaya, M. Naguib, M. Q. Zhao, E. J. Moon, J. Pitock, J. Nanda, S. J. May and Y. Gogotsi, *Adv. Funct. Mater.*, 2016, **26**, 3118–3127.

126 B. Anasori, C. Shi, E. J. Moon, Y. Xie, C. A. Voigt, P. R. Kent, S. J. May, S. J. Billinge, M. W. Barsoum and Y. Gogotsi, *Nanoscale Horiz.*, 2016, **1**, 227–234.

127 Z. Xiao, S. Ruan, L. B. Kong, W. Que, K. Zhou, Y. Liu and T. Zhang, *MXenes and MXenes-based Composites: Processing and Applications*, Springer Nature, 2020.

128 H. Weng, A. Ranjbar, Y. Liang, Z. Song, M. Khazaei, S. Yunoki, M. Arai, Y. Kawazoe, Z. Fang and X. Dai, *Phys. Rev. B: Condens. Matter Mater. Phys.*, 2015, **92**, 075436.

129 M. Khazaei, A. Ranjbar, M. Arai and S. Yunoki, *Phys. Rev. B*, 2016, **94**, 125152.

130 M. Khazaei, M. Arai, T. Sasaki, C. Y. Chung, N. S. Venkataramanan, M. Estili, Y. Sakka and Y. Kawazoe, *Adv. Funct. Mater.*, 2013, **23**, 2185–2192.

131 Q. Tang, Z. Zhou and P. Shen, *J. Am. Chem. Soc.*, 2012, **134**, 16909–16916.

132 L. Dong, H. Kumar, B. Anasori, Y. Gogotsi and V. B. Shenoy, *J. Phys. Chem. Lett.*, 2017, **8**, 422–428.

133 G. Gao, A. P. O'Mullane and A. Du, *ACS Catal.*, 2017, **7**, 494–500.

134 M. Pandey and K. S. Thygesen, *J. Phys. Chem. C*, 2017, **121**, 13593–13598.

135 M. Khazaei, V. Wang, C. Sevik, A. Ranjbar, M. Arai and S. Yunoki, *Phys. Rev. Mater.*, 2018, **2**, 074002.

136 Y. Wang, Y. Xu, M. Hu, H. Ling and X. Zhu, *Nanophotonics*, 2020, **9**, 1601–1620.

137 M. Khazaei, A. Ranjbar, M. Arai, T. Sasaki and S. Yunoki, *J. Mater. Chem. C*, 2017, **5**, 2488–2503.

138 X. Zhan, C. Si, J. Zhou and Z. Sun, *Nanoscale Horiz.*, 2020, **5**, 235–258.

139 L. Hu, X. Wu and J. Yang, *Nanoscale*, 2016, **8**, 12939–12945.

140 G. Wang, *J. Phys. Chem. C*, 2016, **120**, 18850–18857.

141 C. Si, J. Zhou and Z. Sun, *ACS Appl. Mater. Interfaces*, 2015, **7**, 17510–17515.

142 G. Gao, G. Ding, J. Li, K. Yao, M. Wu and M. Qian, *Nanoscale*, 2016, **8**, 8986–8994.

143 D. Xiong, X. Li, Z. Bai and S. Lu, *Small*, 2018, **14**, 1703419.

144 J. He, P. Lyu and P. Nachtigall, *J. Mater. Chem. C*, 2016, **4**, 11143–11149.

145 W. Luo, C. Fang and R. Ahuja, *Condensed Matter Theories: Volume 23*, World Scientific, 2009, pp. 207–211.

146 M. Naguib, T. Saito, S. Lai, M. S. Rager, T. Aytug, M. P. Paranthaman, M.-Q. Zhao and Y. Gogotsi, *RSC Adv.*, 2016, **6**, 72069–72073.

147 Y. Bai, K. Zhou, N. Srikanth, J. H. L. Pang, X. He and R. Wang, *RSC Adv.*, 2016, **6**, 35731–35739.

148 X.-H. Zha, K. Luo, Q. Li, Q. Huang, J. He, X. Wen and S. Du, *EPL*, 2015, **111**, 26007.

149 Z. Guo, J. Zhou, C. Si and Z. Sun, *Phys. Chem. Chem. Phys.*, 2015, **17**, 15348–15354.

150 V. N. Borysiuk, V. N. Mochalin and Y. Gogotsi, *Nanotechnology*, 2015, **26**, 265705.

151 E. A. Mayerberger, O. Urbanek, R. M. McDaniel, R. M. Street, M. W. Barsoum and C. L. Schauer, *J. Appl. Polym. Sci.*, 2017, **134**, 45295.

152 H. Zhang, L. Wang, Q. Chen, P. Li, A. Zhou, X. Cao and Q. Hu, *Mater. Des.*, 2016, **92**, 682–689.

153 M. Khazaei, A. Mishra, N. S. Venkataramanan, A. K. Singh and S. Yunoki, *Curr. Opin. Solid State Mater. Sci.*, 2019, **23**, 164–178.

154 X. Jiang, A. V. Kuklin, A. Baev, Y. Ge, H. Ågren, H. Zhang and P. N. Prasad, *Phys. Rep.*, 2020, **848**, 1–58.

155 M. Mariano, O. Mashtalir, F. Q. Antonio, W.-H. Ryu, B. Deng, F. Xia, Y. Gogotsi and A. D. Taylor, *Nanoscale*, 2016, **8**, 16371–16378.

156 J. Halim, M. R. Lukatskaya, K. M. Cook, J. Lu, C. R. Smith, L.-Å. Näslund, S. J. May, L. Hultman, Y. Gogotsi, P. Eklund and M. W. Barsoum, *Chem. Mater.*, 2014, **26**, 2374–2381.

157 H. Lashgari, M. Abolhassani, A. Boochani, S. Elahi and J. Khodadadi, *Solid State Commun.*, 2014, **195**, 61–69.

158 G. R. Berdiyorov, *AIP Adv.*, 2016, **6**, 055105.

159 K. Hantanasirisakul, M. Q. Zhao, P. Urbankowski, J. Halim, B. Anasori, S. Kota, C. E. Ren, M. W. Barsoum and Y. Gogotsi, *Adv. Electron. Mater.*, 2016, **2**, 1600050.

160 J. Luo, X. Tao, J. Zhang, Y. Xia, H. Huang, L. Zhang, Y. Gan, C. Liang and W. Zhang, *ACS Nano*, 2016, **10**, 2491–2499.

161 J. Ran, G. Gao, F.-T. Li, T.-Y. Ma, A. Du and S.-Z. Qiao, *Nat. Commun.*, 2017, **8**, 13907.

162 B. Anasori, Y. Xie, M. Beidaghi, J. Lu, B. C. Hosler, L. Hultman, P. R. Kent, Y. Gogotsi and M. W. Barsoum, *ACS Nano*, 2015, **9**, 9507–9516.

163 K. Hantanasirisakul and Y. Gogotsi, *Adv. Mater.*, 2018, **30**, 1804779.

164 Y. Chae, S. J. Kim, S.-Y. Cho, J. Choi, K. Maleski, B.-J. Lee, H.-T. Jung, Y. Gogotsi, Y. Lee and C. W. Ahn, *Nanoscale*, 2019, **11**, 8387–8393.

165 T. Habib, X. Zhao, S. A. Shah, Y. Chen, W. Sun, H. An, J. L. Lutkenhaus, M. Radovic and M. J. Green, *NPJ 2D Mater. Appl.*, 2019, **3**, 1–6.

166 Y. T. Liu, P. Zhang, N. Sun, B. Anasori, Q. Z. Zhu, H. Liu, Y. Gogotsi and B. Xu, *Adv. Mater.*, 2018, **30**, 1707334.

167 X. Zhao, A. Vashisth, E. Prehn, W. Sun, S. A. Shah, T. Habib, Y. Chen, Z. Tan, J. L. Lutkenhaus and M. Radovic, *Matter*, 2019, **1**, 513–526.

168 J. Liu, H. B. Zhang, R. Sun, Y. Liu, Z. Liu, A. Zhou and Z. Z. Yu, *Adv. Mater.*, 2017, **29**, 1702367.

169 D. Chen, Y. Zou and S. Wang, *Mater. Today Energy*, 2019, **12**, 250–268.

170 J. Ji, L. Zhao, Y. Shen, S. Liu and Y. Zhang, *FlatChem*, 2019, **17**, 100128.

171 D. Yoo, Y. Kim, M. Min, G. H. Ahn, D.-H. Lien, J. Jang, H. Jeong, Y. Song, S. Chung and A. Javey, *ACS Nano*, 2018, **12**, 11062–11069.

172 Y. Lee, S. Bae, B. Hwang, M. Schroeder, Y. Lee and S. Baik, *J. Mater. Chem. C*, 2019, **7**, 12297–12305.

173 W. Y. Chen, S.-N. Lai, C.-C. Yen, X. Jiang, D. Peroulis and L. A. Stanciu, *ACS Nano*, 2020, **14**, 11490–11501.

174 X. Wang, H. Li, H. Li, S. Lin, W. Ding, X. Zhu, Z. Sheng, H. Wang, X. Zhu and Y. Sun, *Adv. Funct. Mater.*, 2020, **30**, 0190302.

175 H. Zhang, M. Li, J. Cao, Q. Tang, P. Kang, C. Zhu and M. Ma, *Ceram. Int.*, 2018, **44**, 19958–19962.

176 P. Kuang, M. He, B. Zhu, J. Yu, K. Fan and M. Jaroniec, *J. Catal.*, 2019, **375**, 8–20.

177 J. Qin, X. Hu, X. Li, Z. Yin, B. Liu and K.-H. Lam, *Nano Energy*, 2019, **61**, 27–35.

178 C. Xing, S. Chen, M. Qiu, X. Liang, Q. Liu, Q. Zou, Z. Li, Z. Xie, D. Wang and B. Dong, *Adv. Healthcare Mater.*, 2018, **7**, 1870030.

179 C. Dai, Y. Chen, X. Jing, L. Xiang, D. Yang, H. Lin, Z. Liu, X. Han and R. Wu, *ACS Nano*, 2017, **11**, 12696–12712.

180 W. Tang, Z. Dong, R. Zhang, X. Yi, K. Yang, M. Jin, C. Yuan, Z. Xiao, Z. Liu and L. Cheng, *ACS Nano*, 2018, **13**, 284–294.

181 Y. Jiang, X. Zhang, L. Pei, S. Yue, L. Ma, L. Zhou, Z. Huang, Y. He and J. Gao, *Chem. Eng. J.*, 2018, **339**, 547–556.

182 F. Wang, C. Yang, C. Duan, D. Xiao, Y. Tang and J. Zhu, *J. Electrochem. Soc.*, 2014, **162**, B16.

183 H. Liu, C. Duan, C. Yang, W. Shen, F. Wang and Z. Zhu, *Sens. Actuators, B*, 2015, **218**, 60–66.

184 R. Rakhi, P. Nayak, C. Xia and H. N. Alshareef, *Sci. Rep.*, 2016, **6**, 1–10.

185 K. S. Naunheim, P. J. Petruska, T. S. Roy, C. H. Andrus, F. E. Johnson, J. M. Schlueter and A. E. Baue, *J. Thorac. Cardiovasc. Surg.*, 1992, **103**, 887–895.

186 M. S. Piver, J. J. Barlow, F. T. Lee and V. Vongtama, *Am. J. Obstet. Gynecol.*, 1975, **122**, 355–357.

187 J. T. Robinson, S. M. Tabakman, Y. Liang, H. Wang, H. Sanchez Casalongue, D. Vinh and H. Dai, *J. Am. Chem. Soc.*, 2011, **133**, 6825–6831.

188 A. Bashkatov, E. Genina, V. Kochubey and V. Tuchin, *J. Phys. D: Appl. Phys.*, 2005, **38**, 2543.

189 D. J. Slamon, B. Leyland-Jones, S. Shak, H. Fuchs, V. Paton, A. Bajamonde, T. Fleming, W. Eiermann, J. Wolter and M. Pegram, *N. Engl. J. Med.*, 2001, **344**, 783–792.

190 T. Ide, S. Hirabayashi, S. Kano and M. Sugano, *Biochim. Biophys. Acta, Lipids Lipid Metab.*, 1992, **1124**, 163–170.

191 Y.-Z. Zhang, K. H. Lee, D. H. Anjum, R. Sougrat, Q. Jiang, H. Kim and H. N. Alshareef, *Sci. Adv.*, 2018, **4**, eaat0098.

192 X. Shi, H. Wang, X. Xie, Q. Xue, J. Zhang, S. Kang, C. Wang, J. Liang and Y. Chen, *ACS Nano*, 2018, **13**, 649–659.

193 Y. Cai, J. Shen, G. Ge, Y. Zhang, W. Jin, W. Huang, J. Shao, J. Yang and X. Dong, *ACS Nano*, 2018, **12**, 56–62.

194 L. Lorencova, V. Gajdosova, S. Hroncekova, T. Bertok, J. Blahutova, A. Vikartovska, L. Parrakova, P. Gemeiner, P. Kasak and J. Tkac, *Electroanalysis*, 2019, **31**, 1833–1844.

195 X. Chen, J. Li, G. Pan, W. Xu, J. Zhu, D. Zhou, D. Li, C. Chen, G. Lu and H. Song, *Sens. Actuators, B*, 2019, **289**, 131–137.

196 J. Liu, X. Jiang, R. Zhang, Y. Zhang, L. Wu, W. Lu, J. Li, Y. Li and H. Zhang, *Adv. Funct. Mater.*, 2019, **29**, 1807326.

197 W. Yuan, K. Yang, H. Peng, F. Li and F. Yin, *J. Mater. Chem. A*, 2018, **6**, 18116–18124.

198 F. Wang, C. Yang, M. Duan, Y. Tang and J. Zhu, *Biosens. Bioelectron.*, 2015, **74**, 1022–1028.

199 B. Shao, J. Wang, Z. Liu, G. Zeng, L. Tang, Q. Liang, Q. He, T. Wu, Y. Liu and X. Yuan, *J. Mater. Chem. A*, 2020, **8**, 5171–5185.

200 H. Wang, Y. Wu, T. Xiao, X. Yuan, G. Zeng, W. Tu, S. Wu, H. Y. Lee, Y. Z. Tan and J. W. Chew, *Appl. Catal., B*, 2018, **233**, 213–225.

201 V. Ramalingam, P. Varadhan, H. C. Fu, H. Kim, D. Zhang, S. Chen, L. Song, D. Ma, Y. Wang and H. N. Alshareef, *Adv. Mater.*, 2019, **31**, 1903841.

202 Y. Zheng, Y. Jiao, Y. Zhu, L. H. Li, Y. Han, Y. Chen, M. Jaroniec and S.-Z. Qiao, *J. Am. Chem. Soc.*, 2016, **138**, 16174–16181.

203 J. Kibsgaard, T. F. Jaramillo and F. Besenbacher, *Nat. Chem.*, 2014, **6**, 248.

204 W. Yuan, L. Cheng, Y. An, H. Wu, N. Yao, X. Fan and X. Guo, *ACS Sustainable Chem. Eng.*, 2018, **6**, 8976–8982.

205 Q. Zhu, Y. Cui, Y. Zhang, Z. Cao, Y. Shi, J. Gu, Z. Du, B. Li and S. Yang, *Mater. Today Nano*, 2021, **13**, 100104.

206 J. Zhang, L. Yang, H. Wang, G. Zhu, H. Wen, H. Feng, X. Sun, X. Guan, J. Wen and Y. Yao, *Inorg. Chem.*, 2019, **58**, 5414–5418.

207 J. Low, L. Zhang, T. Tong, B. Shen and J. Yu, *J. Catal.*, 2018, **361**, 255–266.

208 Y. Gao, L. Wang, A. Zhou, Z. Li, J. Chen, H. Bala, Q. Hu and X. Cao, *Mater. Lett.*, 2015, **150**, 62–64.

209 T. Su, R. Peng, Z. D. Hood, M. Naguib, I. N. Ivanov, J. K. Keum, Z. Qin, Z. Guo and Z. Wu, *ChemSusChem*, 2018, **11**, 688–699.

210 H. Wang, R. Zhao, J. Qin, H. Hu, X. Fan, X. Cao and D. Wang, *ACS Appl. Mater. Interfaces*, 2019, **11**, 44249–44262.

211 M. Yu, S. Zhou, Z. Wang, J. Zhao and J. Qiu, *Nano Energy*, 2018, **44**, 181–190.

212 C. F. Du, X. Sun, H. Yu, Q. Liang, K. N. Dinh, Y. Zheng, Y. Luo, Z. Wang and Q. Yan, *Adv. Sci.*, 2019, **6**, 1900116.

213 B.-Z. Zhan, M. A. White, T.-K. Sham, J. A. Pincock, R. J. Doucet, K. R. Rao, K. N. Robertson and T. S. Cameron, *J. Am. Chem. Soc.*, 2003, **125**, 2195–2199.

214 S. Cheng, H. Liu and B. E. Logan, *Environ. Sci. Technol.*, 2006, **40**, 364–369.

215 Y. Tang, C. Yang, Y. Tian, Y. Luo, X. Yin and W. Que, *Nanoscale Adv.*, 2020, **2**, 1187–1194.

216 D. A. Kuznetsov, Z. Chen, P. V. Kumar, A. Tsoukalou, A. Kierzkowska, P. M. Abdala, O. V. Safonova, A. Fedorov and C. R. Müller, *J. Am. Chem. Soc.*, 2019, **141**, 17809–17816.

217 J. Zhang, Y. Zhao, X. Guo, C. Chen, C.-L. Dong, R.-S. Liu, C.-P. Han, Y. Li, Y. Gogotsi and G. Wang, *Nat. Catal.*, 2018, **1**, 985–992.

218 M. Naguib, J. Come, B. Dyatkin, V. Presser, P.-L. Taberna, P. Simon, M. W. Barsoum and Y. Gogotsi, *Electrochem. Commun.*, 2012, **16**, 61–64.

219 Y.-Y. Peng, B. Akuzum, N. Kurra, M.-Q. Zhao, M. Alhabeb, B. Anasori, E. C. Kumbur, H. N. Alshareef, M.-D. Ger and Y. Gogotsi, *Energy Environ. Sci.*, 2016, **9**, 2847–2854.

220 Y. Song, Z. Sun, Z. Fan, W. Cai, Y. Shao, G. Sheng, M. Wang, L. Song, Z. Liu and Q. Zhang, *Nano Energy*, 2020, **70**, 104555.

221 H. Yu, Y. Wang, Y. Jing, J. Ma, C.-F. Du and Q. Yan, *Small*, 2019, **15**, 1901503.

222 M. Ghidiu, J. Halim, S. Kota, D. Bish, Y. Gogotsi and M. W. Barsoum, *Chem. Mater.*, 2016, **28**, 3507–3514.

223 M. Ghidiu, M. R. Lukatskaya, M.-Q. Zhao, Y. Gogotsi and M. W. Barsoum, *Nature*, 2014, **516**, 78–81.

224 X. Tang, X. Guo, W. Wu and G. Wang, *Adv. Energy Mater.*, 2018, **8**, 1801897.

225 C. Eames and M. S. Islam, *J. Am. Chem. Soc.*, 2014, **136**, 16270–16276.

226 V. Etacheri, R. Marom, R. Elazari, G. Salitra and D. Aurbach, *Energy Environ. Sci.*, 2011, **4**, 3243–3262.

227 J. Huang, R. Meng, L. Zu, Z. Wang, N. Feng, Z. Yang, Y. Yu and J. Yang, *Nano Energy*, 2018, **46**, 20–28.

228 B. Ahmed, D. H. Anjum, M. N. Hedhili, Y. Gogotsi and H. N. Alshareef, *Nanoscale*, 2016, **8**, 7580–7587.

229 W. Lv, J. Zhu, F. Wang and Y. Fang, *J. Mater. Sci.: Mater. Electron.*, 2018, **29**, 4881–4887.

230 C. Yang, Y. Liu, X. Sun, Y. Zhang, L. Hou, Q. Zhang and C. Yuan, *Electrochim. Acta*, 2018, **271**, 165–172.

231 C. Wang, S. Chen, H. Xie, S. Wei, C. Wu and L. Song, *Adv. Energy Mater.*, 2019, **9**, 1802977.

232 X. Guo, W. Zhang, J. Zhang, D. Zhou, X. Tang, X. Xu, B. Li, H. Liu and G. Wang, *ACS Nano*, 2020, **14**, 3651–3659.

233 V. Natu, R. Pai, M. Sokol, M. Carey, V. Kalra and M. W. Barsoum, *Chem*, 2020, **6**, 616–630.

234 A. Uihlein and D. Magagna, *Renewable Sustainable Energy Rev.*, 2016, **58**, 1070–1081.

235 C. S. Ponseca Jr, P. Chabera, J. Uhlig, P. Persson and V. Sundstrom, *Chem. Rev.*, 2017, **117**, 10940–11024.

236 X. Liu, X. Jin, L. Li, J. Wang, Y. Yang, Y. Cao and W. Wang, *J. Mater. Chem. A*, 2020, **8**, 12526–12537.

237 Y. Yang, R. Zhao, T. Zhang, K. Zhao, P. Xiao, Y. Ma, P. M. Ajayan, G. Shi and Y. Chen, *ACS Nano*, 2018, **12**, 829–835.

238 Z. Zha, X. Yue, Q. Ren and Z. Dai, *Adv. Mater.*, 2013, **25**, 777–782.

239 D. Yang, B. Zhou, G. Han, Y. Feng, J. Ma, J. Han, C. Liu and C. Shen, *ACS Appl. Mater. Interfaces*, 2021, **13**, 8909–8918.

240 X. Du, J. Qiu, S. Deng, Z. Du, X. Cheng and H. Wang, *ACS Sustainable Chem. Eng.*, 2020, **8**, 5799–5806.

241 X. Fan, Y. Ding, Y. Liu, J. Liang and Y. Chen, *ACS Nano*, 2019, **13**, 8124–8134.

242 Y. A. Al-Hamadani, B.-M. Jun, M. Yoon, N. Taheri-Qazvini, S. A. Snyder, M. Jang, J. Heo and Y. Yoon, *Chemosphere*, 2020, 126821.

243 X. Li, Y. Liu, J. Wang, J. Gascon, J. Li and B. Van der Bruggen, *Chem. Soc. Rev.*, 2017, **46**, 7124–7144.

244 A. Sinha, H. Zhao, Y. Huang, X. Lu, J. Chen and R. Jain, *TrAC, Trends Anal. Chem.*, 2018, **105**, 424–435.

245 A. Arabi Shamsabadi, M. Sharifian Gh, B. Anasori and M. Soroush, *ACS Sustainable Chem. Eng.*, 2018, **6**, 16586–16596.

246 H. B. Park, J. Kamcev, L. M. Robeson, M. Elimelech and B. D. Freeman, *Science*, 2017, **356**, 1138–1148.

247 K. Guan, F. Liang, H. Zhu, J. Zhao and W. Jin, *ACS Appl. Mater. Interfaces*, 2018, **10**, 13903–13913.

248 L. Ding, Y. Wei, Y. Wang, H. Chen, J. Caro and H. Wang, *Angew. Chem., Int. Ed.*, 2017, **56**, 1825–1829.

249 M. Naguib, M. Kurtoglu, V. Presser, J. Lu, J. Niu, M. Heon, L. Hultman, Y. Gogotsi and M. W. Barsoum, *Adv. Mater.*, 2011, **23**, 4248–4253.

250 G. Liu, S. Liu, K. Ma, H. Wang, X. Wang, G. Liu and W. Jin, *Ind. Eng. Chem. Res.*, 2020, **59**, 4732–4741.

251 J. G. Wijmans and R. W. Baker, *J. Membr. Sci.*, 1995, **107**, 1–21.

252 C. S. Lee, M. k. Choi, Y. Y. Hwang, H. Kim, M. K. Kim and Y. J. Lee, *Adv. Mater.*, 2018, **30**, 1705944.

253 L. Hao, H. Zhang, X. Wu, J. Zhang, J. Wang and Y. Li, *Composites, Part A*, 2017, **100**, 139–149.

254 J. Fei, S. W. Koh, W. Tu, J. Ge, H. Rezaeyan, S. Hou, H. Duan, Y. C. Lam and H. Li, *Adv. Sustainable Syst.*, 2020, **4**, 2000102.

255 L. Ding, L. Li, Y. Liu, Y. Wu, Z. Lu, J. Deng, Y. Wei, J. Caro and H. Wang, *Nat. Sustainable*, 2020, **3**, 296–302.

256 I. Ihsanullah, *Nano-Micro Lett.*, 2020, **12**, 1–20.

257 C. E. Ren, K. B. Hatzell, M. Alhabeb, Z. Ling, K. A. Mahmoud and Y. Gogotsi, *J. Phys. Chem. Lett.*, 2015, **6**, 4026–4031.

258 M. Rezakazemi, A. A. Shamsabadi, H. Lin, P. Luis, S. Ramakrishna and T. M. Aminabhavi, *Renewable Sustainable Energy Rev.*, 2021, **143**, 110878.

259 R. Li, L. Zhang, L. Shi and P. Wang, *ACS Nano*, 2017, **11**, 3752–3759.

260 K. Vikrant, B. S. Giri, N. Raza, K. Roy, K.-H. Kim, B. N. Rai and R. S. Singh, *Bioresour. Technol.*, 2018, **253**, 355–367.

261 B.-M. Jun, N. Her, C. M. Park and Y. Yoon, *Environ. Sci.: Water Res. Technol.*, 2020, **6**, 173–180.

262 Y. Du, B. Yu, L. Wei, Y. Wang, X. Zhang and S. Ye, *J. Mater. Sci.*, 2019, **54**, 13283–13297.

263 R. P. Pandey, K. Rasool, V. E. Madhavan, B. Aïssa, Y. Gogotsi and K. A. Mahmoud, *J. Mater. Chem. A*, 2018, **6**, 3522–3533.

264 J. Shen, G. Liu, Y. Ji, Q. Liu, L. Cheng, K. Guan, M. Zhang, G. Liu, J. Xiong and J. Yang, *Adv. Funct. Mater.*, 2018, **28**, 1801511.

265 C. Ma and J. J. Urban, *Proc. Natl. Res. Soc.*, 2018, **2**, 2002.

266 M. Mozafari, R. Abedini and A. Rahimpour, *J. Mater. Chem. A*, 2018, **6**, 12380–12392.

267 M. Mozafari, A. Rahimpour and R. Abedini, *J. Ind. Eng. Chem.*, 2020, **85**, 102–110.

268 S. Yuan, X. Li, J. Zhu, G. Zhang, P. Van Puyvelde and B. Van der Bruggen, *Chem. Soc. Rev.*, 2019, **48**, 2665–2681.

269 C. Y. Chuah, J. Lee, Y. Bao, J. Song and T.-H. Bae, *J. Membr. Sci.*, 2021, **622**, 119031.

270 N. Nidamanuri, Y. Li, Q. Li and M. Dong, *Eng. Sci.*, 2020, **9**, 3–16.

271 J. Zhu, J. Hou, A. Uliana, Y. Zhang, M. Tian and B. Van der Bruggen, *J. Mater. Chem. A*, 2018, **6**, 3773–3792.

272 L. Ding, Y. Wei, L. Li, T. Zhang, H. Wang, J. Xue, L.-X. Ding, S. Wang, J. Caro and Y. Gogotsi, *Nat. Commun.*, 2018, **9**, 1–7.